Final Technical Report

on

INFRARED SIGNATURE MASKING BY AIR PLASMA RADIATION

Grant No. NAG 2-1079

Prepared for

NATIONAL AERONAUTICS AND SPACE ADMINISTRATION

For the Period

June 1, 1997 to October 31, 2000

Submitted by

C. H. Kruger, Principal Investigator
C. O. Laux, Associate Investigator

March 2001

Contents

1. Introduction

This report summarizes the results obtained during a research program on the infrared radiation of air plasmas conducted in the High Temperature Gasdynamics Laboratory at Stanford University under the direction of Professor Charles H. Kruger, with Dr. Christophe O. Laux as Associate Investigator. This program was supported by a grant from the Ballistic Missile Defense Organization (Technical Monitor: Dr. David Mann) and funded through the National Aeronautics and Space Administration (NAG 2-1079) with Dr. Winifred Huo from NASA-Ames as Technical Monitor. One Ph.D. student, Richard J. Gessman, graduated from this program. Dr. Laurent Pierrot, Postdoctoral Fellow, and Denis Packan, who is currently pursuing a Ph.D program, also contributed to the research presented here.

The goal of the research was to investigate the masking of infrared signatures by the air plasma formed behind the bow shock of high velocity missiles. To this end, spectral measurements and modeling were made of the radiation emitted between 2.4 and 5.5 μm by an atmospheric pressure air plasma in chemical and thermal equilibrium at a temperature of approximately 3000 K. The objective was to examine the spectral emission of air species including nitric oxide, atomic oxygen and nitrogen lines, molecular and atomic continua, as well as secondary species such as water vapor or carbon dioxide. The cold air stream injected in the plasma torch contained approximately 330 parts per million of CO_2, which is the natural CO_2 concentration in atmospheric air at room temperature, and a small amount of water vapor with an estimated mole fraction of 3.8×10^{-4}.

The measurements, shown in Figure 1, demonstrate that infrared signatures are masked by the interceptor's bow-shock between 4.15 and 5.5 μm, owing to intense emission from the fundamental rovibrational bands of NO at 4.9-5.5 μm and the ν_3 band of CO_2 (antisymmetric stretch) at 4.2-4.8 μm. The measurements also show that emission bands of OH and NO (first overtone) produce intense features between 2.5 and 3.5 μm. The spectral range 3.5-4.15 μm is the most transparent region. As these spectral measurements were made in an LTE plasma with known species concentrations and temperature, comparisons were made with equilibrium numerical predictions obtained with the NEQAIR2-IR code which was subsequently extended to model the observed transitions. This effort resulted in an accurate predictive tool for the infrared radiation of air plasmas. Results relative to the measurement and modeling of the molecular radiation of equilibrium air plasmas in the infrared are summarized in Section 2 of the report.

To extend the predictive capabilities to higher temperature bow shock plasmas wherein atomic lines and continuum radiation may produce additional radiation, a detailed analysis was made of the various continua and atomic lines that contribute to the infrared emission spectrum. Results are presented in Section 3 of this report. In particular, detailed

comparisons are shown of atomic line measurements and predictions in the range 0.8-5 micron.

Section 4 of the report presents our investigations of the effects of thermal and chemical nonequilibrium on the radiation of nitrogen plasmas. Spectroscopic measurements were made in a nonequilibrium recombining nitrogen/argon plasma produced by rapid cooling in a controlled environment. A detailed collisional-radiative model of nitrogen comprising 360 rovibrational and electronic states of neutral and ionic nitrogen atoms and molecules was developed. Over 11000 reactions between individual levels were considered. This work represents the first comprehensive model of ground and excited nitrogen chemical kinetics. This model provides a basis for modeling nonequilibrium radiation that could be extended in future work to the modeling of the nonequilibrium infrared radiation of air plasmas.

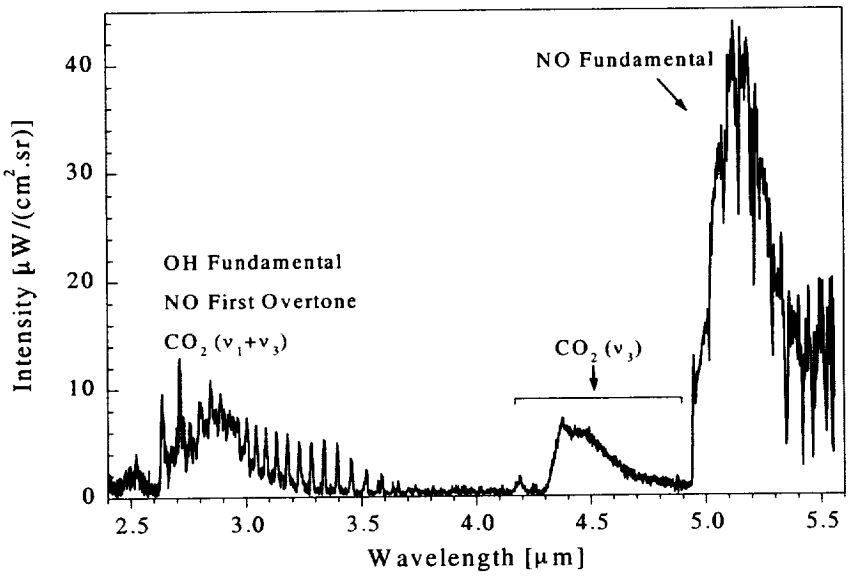

Figure 1. Measured IR emission spectrum (present work): P=1 atm, maximum plasma temperature = ~3400K.

2. Measurements and Modeling of NO, OH, and CO_2 Infrared Radiation in Low Temperature Air Plasmas

2.1. Experimental Setup and Conditions

The experimental work was conducted with a 50 kW TAFA model 66 RF induction plasma torch powered by a LEPEL model T-50-3 power supply operating at a frequency of 4 MHz. As shown in Figure 2, a copper nozzle of 1.0-cm exit diameter was utilized at the top of the upward firing torch, and the plasma was cooled by flowing through a water-cooled brass test section 60 cm in length. All measurements were made 1 cm downstream of the exit of the test section, in a region where the flow is laminar.

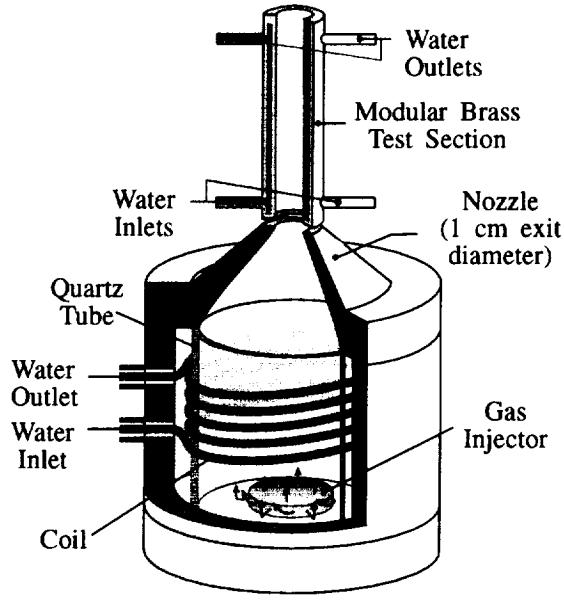

Figure 2. Torch head schematic, presented here with a ~20 cm-long test section instead of the 60 cm-long used in the experiment.

The set-up for spectral measurements includes a SPEX model 750M 3/4 meter scanning monochromator fitted with a Cincinnati Electronics model SDD-20E1-S1 indium-antimonide cryogenically-cooled (liquid N_2) infrared detector with integrated pre-amplifier. A 300-grooves/mm grating blazed at 4.0 μm was used at first order, and higher order spectra were rejected by using two long-pass filters with cut-offs at 1.5 μm and 3.0 μm, respectively. The monochromator entrance slit was 1 mm and the exit slit 2.8 mm.

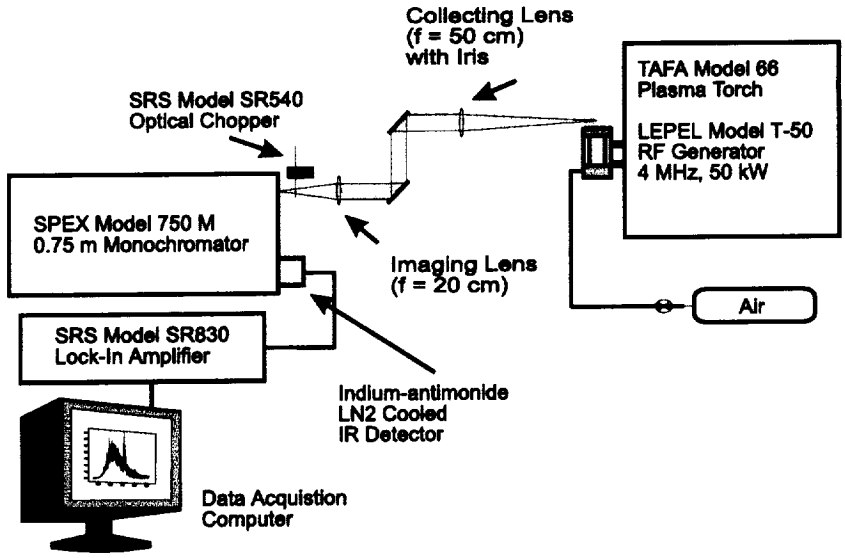

Figure 3. Setup for optical diagnostics.

The air injected into the torch contained approximately 330 ppm of CO_2 and 4.5×10^{-3} mole fraction of water vapor. The temperature and humidity in room air were recorded during the experiment and calibration. In both cases, the measured ambient temperature was 25°C and the relative humidity was 42% (10% uncertainty), which correspond to a mole fraction of H_2O of 0.013±0.001 (Reynolds and Perkins [1], p. 622).

The spectral range of the measurements covered 2.4 – 5.6 μm so as to capture NO first overtone and OH fundamental rovibrational bands. The measured temperature profile was obtained from Abel-inverted profiles of absolute NO (1-0) bandhead intensities. The temperature profile had a maximum value of 3400 K at the center of the plasma plume. The plasma produced by the torch under the present conditions was found to be close to Local Thermodynamic Equilibrium (LTE) in previous work [2]. The concentrations of the different species used in the simulations were therefore calculated by assuming chemical equilibrium at atmospheric pressure and at the measured temperatures. The mole fractions of the main species are plotted in Figure 4, along with the measured temperature profile.

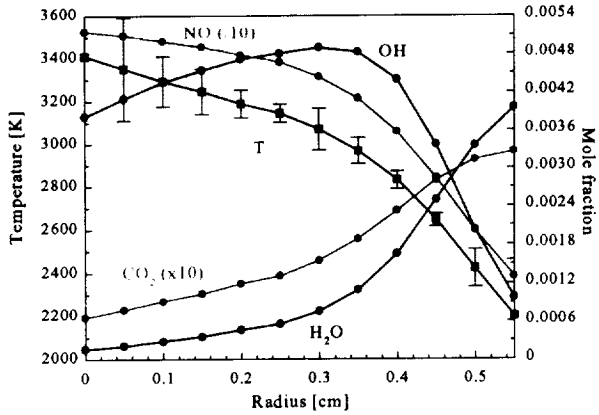

Figure 4. Radial temperature and mole fraction profiles at the exit of the test section.

Spectral Calibration

Absolute intensity calibrations were made using an Optronics Laboratories calibrated tungsten lamp (model OL550) traceable to NIST standards. Water vapor and carbon dioxide present over the 6-meter long optical path that separates the plasma source or calibration lamp from the detector can absorb a significant fraction of emission between 1.5 and 2.9 μm and at wavelengths ≥ 4.0 μm. Both the calibration signal and the experimental spectrum were affected by room-air absorption.

It may be thought possible to recover the calibrated plasma torch emission spectrum by simply dividing the measured plasma torch signal by the calibration signal. Such a procedure would be flawed as absorption lines of room air may occur at different wavelengths than plasma emission lines. In other words, the absorption lines of room-air water vapor and carbon dioxide always contribute to absorption features in the calibration spectrum, because of the continuum nature of the emission of the calibration lamp, but do not necessarily absorb plasma emission. This is illustrated in Figure 5, which shows a small portion of the emission spectrum of NO fundamental before convolution (bottom curve), along with a plot of the spectral transmittance of 6 meters of room air (top curve). The H_2O lines at 30449 Å and 30460 Å, for example, fall in between NO emission lines and thus do not absorb plasma emission, but absorb the continuous emission of the calibration lamp at these wavelengths. Therefore the corresponding absorption feature in the calibration spectrum does not appear and should not be corrected for in the plasma spectrum.

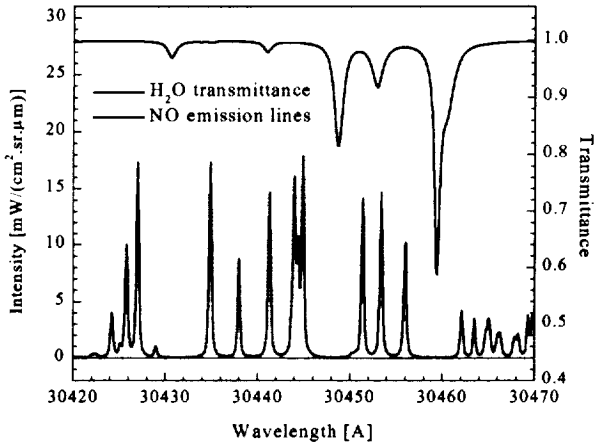

Figure 5. NO fundamental emission lines and room-air transmittance.

The correct procedure to calibrate the spectrum is to deconvolve room air absorption from the calibration signal, and then to divide the plasma emission signal by the corrected (i.e. room-air absorption-corrected) calibration signal. With this procedure, the calibrated plasma spectrum represents the spectrum emitted by the plasma and absorbed by room air, and the absorption features of water vapor and carbon dioxide remain part of the experimental emission spectrum. In order to model this spectrum, it is then necessary to determine the

spectral emission of the plasma and then solve the transport equation over a path of room air. The deconvolution procedure is presented next.

Deconvolution of room-air absorption features in the calibration signal:

The raw calibration signal (detector voltage) is shown in Figure 6. Absorption features of room air species (CO_2 and H_2O) are indicated. Absorption by CO_2 at 4.3 μm can be removed by a straight line interpolation. This approximation is valid because the OL550 tungsten filament emission and the grating response vary smoothly in that spectral range. The other absorption features occur over wider wavelength ranges and cannot be deconvolved using such a simple procedure. For these features, our deconvolution procedure consists in dividing the calibration signal by the spectral transmission spectrum (convolved with the instrumental slit function) of room air. The transmission spectrum of room air was obtained with the HITRAN96 database [3] with the following parameters: room temperature of 298 K, optical path-length through room air equal to 6 meters, H_2O mole fraction of 0.013 and CO_2 mole fraction of 330 ppm. Figure 7 and Figure 8 show the calculated contributions of water vapor and carbon dioxide, respectively, to the transmittance of a 6 meter room-air path.

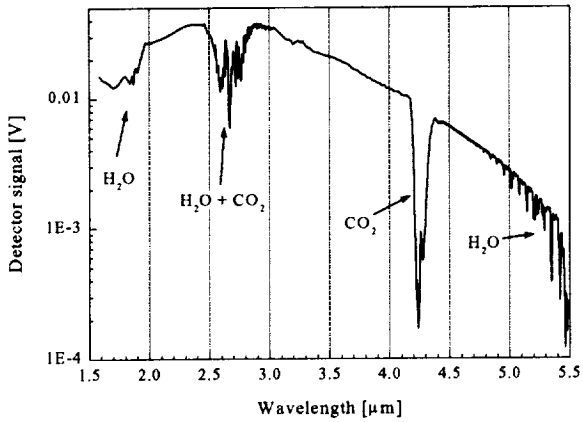

Figure 6. Raw calibration spectrum obtained with the OL550 calibration standard.

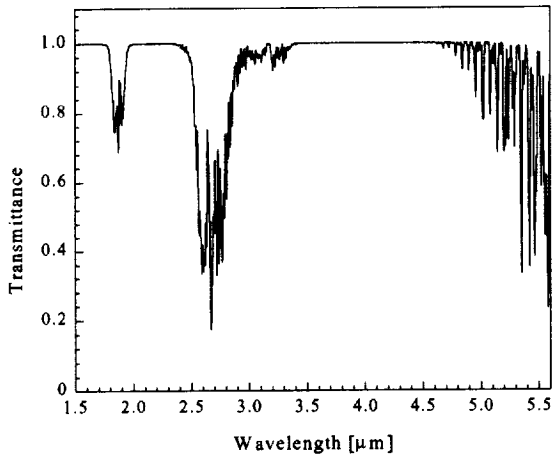

Figure 7. Calculated H_2O contribution to the spectral transmittance of 6 meters of room air.

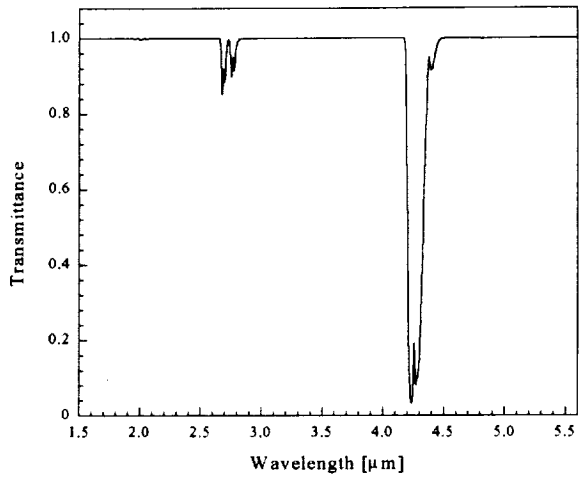

Figure 8. Calculated CO_2 contribution to the spectral transmittance of 6 meters of room air.

Results of the deconvolution procedure around 1.8 and 2.7 μm are shown in Figure 9. The red curve represents the corrected calibration using the spectral absorption coefficient determined with HITRAN. As can be seen in Figure 9, the deconvolution procedure at 1.8 μm produces a smoothly-varying trace. At 2.7 μm, the recovered spectrum still shows residual H_2O absorption lines which cannot be removed by varying the H_2O mole fraction. We believe that these residual features could be due to inaccuracies in the HITRAN database or to uncertainties on the instrumental slit-function, which was deduced from the entrance and exit slit widths and the theoretical reciprocal linear dispersion of the monochromator [4]. In future work, the slit functions will be measured experimentally with a monochromatic light source to increase the accuracy of the deconvolution procedure. The recovered calibration spectrum between 2.5 μm and 3.0 μm shows a cusp and an S-shape variation that is likely due to the spectral response of the ruled grating. Since the grating spectral response should be relatively smooth, we replaced the part of the red curve between 2.5 and 3.0 μm with a fourth order polynomial fit (blue curve).

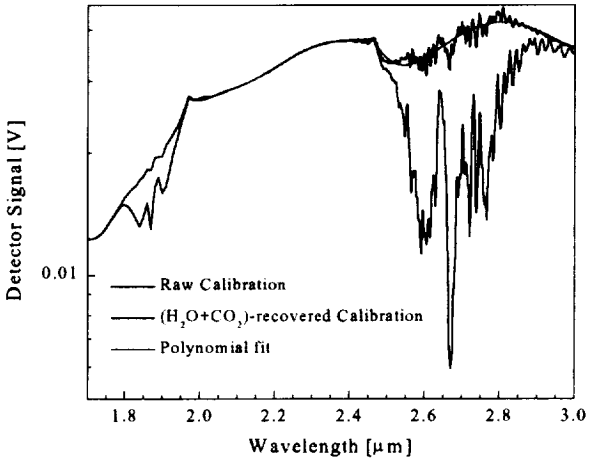

Figure 9. Absorption-deconvolved calibration spectrum in range 1.7-3.0 μm (The absorption features are due to room air H_2O and CO_2).

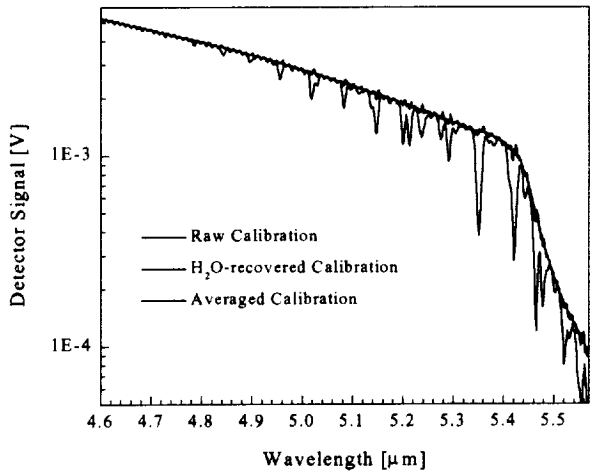

Figure 10. Absorption-deconvolved calibration spectrum in range 4.6-5.6 μm (The absorption features are due to room air H_2O).

Results of the deconvolution procedure between 4.5 μm and 5.5 μm are presented in Figure 10. In this range, room air absorption is mostly due to H_2O. As can be seen from the figure, the deconvolved calibration signal exhibits smooth variations in this spectral range. The small oscillations on the red curve are due to etalonning interference by the quartz window of the tungsten calibration lamp. These oscillations were finally smoothed out using adjacent averaging (blue curve). Figure 11 shows the summary comparison between the raw calibration spectrum and the deconvolved calibration spectrum.

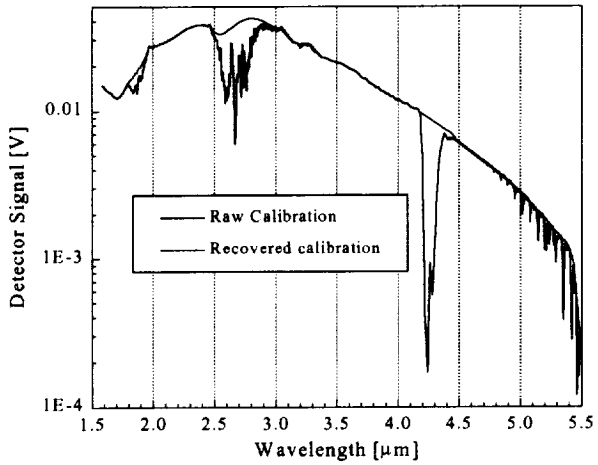

Figure 11. Calibration spectrum corrected for water vapor and carbon dioxide absorption.

2.2. Radiation Model

The measured emission spectrum, corrected for the spectral response of the detection system and calibrated in absolute intensity using the procedure discussed in the foregoing section, is presented in Figure 12.

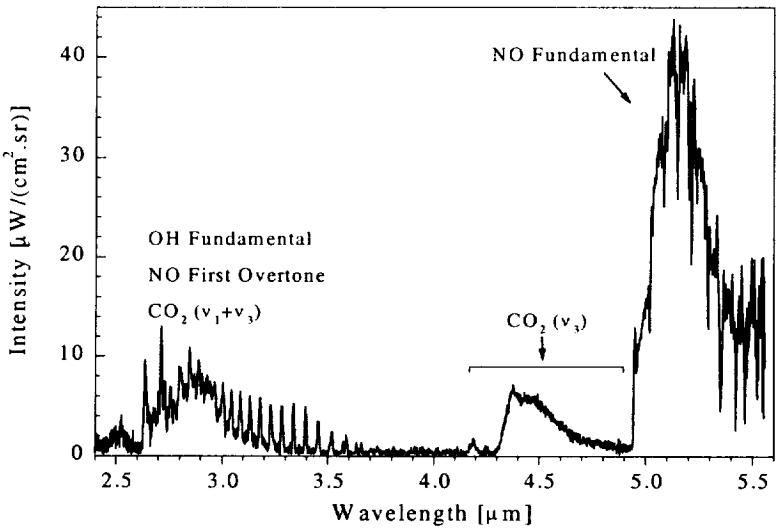

Figure 12. Measured IR emission spectrum (present work: P=1 atm, maximum plasma temperature = ~3400K).

The spectrum shows the fundamental bands of NO at ~5 μm, the ν_3 band of CO_2 around 4.3 μm, and the lines of OH fundamental and of the NO first overtone ($\Delta v=2$) along with the ($\nu_1+\nu_3$) band of CO_2 between 2.5 μm and 4.15 μm. We summarize next our modeling efforts for these radiative transitions.

2.2.1. NO rovibrational bands

The fundamental ($\Delta v = 1$) and first overtone ($\Delta v = 2$) rovibrational bands of NO ($X^2\Pi$) are clearly seen in the experimental spectrum shown in Figure 12. A detailed, accurate model of fundamental and overtone bands of NO ($X^2\Pi$) was implemented in NEQAIR2-IR, as previously described in Ref. [4]. The code determines rotational line positions by diagonalizing the Hamiltonian of Amiot [5]. For each vibrational band, vibrational dipole moments $M_{v'v''}$ defined as:

$$\left(M_{v'v''}\right)^2 = \left(\int \Psi_{v'}(r) D_e(r) \Psi_{v''}(r) dr\right)^2,$$

where D_e stands for the electric dipole moment function (EDMF), were determined using the accurate *ab initio* EDMF of Langhoff *et al.*[6]. The Hönl-London factor expressions (corresponding to Hund's case *a*) recommended by Spencer *et al.*[7] were employed. The model provides accurate line intensities and spectral positions, which are of particular importance for high-resolution spectroscopic diagnostics and for the accurate simulation of absorption of fundamental and overtone NO bands by atmospheric water vapor.

2.2.2. *CO_2 bands: ν_3 antisymmetric stretch at 4.3 μm and (ν_1+ν_3) band at 2.7 μm*

Computations of the CO_2 band spectrum at 2.7 and 4.3 μm were obtained with a *correlated-k* model [8] for CO_2 implemented by Pierrot *et al.* [9]. The *correlated-k* model is a narrow-band model in which the actual spectrum is replaced on each narrow band by the reordered spectrum, so that the spectral integration is carried out using typically 10 points instead of several thousands. In the case of CO_2 infrared radiation, this model affords radiative intensity predictions within a few percent accuracy [10]. The parameters used for the simulations presented in this paper are based on a 16-point Gaussian quadrature and a spectral decomposition over intervals of width 25 cm^{-1}.

2.2.3. *OH rovibrational bands*

The fundamental ($\Delta v = 1$) bands of OH ($X^2\Pi$) are clearly seen between 2.5 and 4 μm in the experimental spectrum shown in Figure 13. As for the NO infrared bands, an accurate line-by-line model of fundamental (and overtone) bands of OH ($X^2\Pi$) was incorporated in NEQAIR2-IR. Rovibrational term energies and line positions for the 1-0 and 2-1 bands of this transition are determined by diagonalizing the Hamiltonian of Stark *et al.* [11] (with corrections of Levin *et al.* [12]). As for the case of NO infrared bands, this model provides the highly accurate spectral positions required for reliable simulations of absorption by atmospheric water vapor. In future work, we also intend to incorporate additional bands originating in higher vibrational levels, with line positions for these levels determined using the parameters of Coxon.[13]

Transition probabilities of the OH infrared lines have a very strong dependence on centrifugal distortions of the vibrational potentials. As a result, the P and R branches show an anomalous distribution with intense P branches (2.6 to 4.0 μm) and very weak R branches (2.4 to 2.6 μm). In the NEQAIR2-IR model, we utilized the P- and R-branch transition probabilities determined by Holtzclaw *et al.*[14].

2.2.4. *Room air absorption*

The HITRAN96 database [3] was used to determine the transmittance spectrum of room air over a 6-meter optical path. CO_2 concentration was taken equal to 300 ppm. An H_2O mole fraction of 0.014 was used. The procedure for taking into account absorption is as follows: first, the emission spectrum of the plasma is computed at high spectral resolution (10 points per angström, or approximately 10 points per line). Then, attenuation of this spectrum by water vapor and carbon dioxide absorption is determined with Beer's law, using the line strengths and spectral broadening coefficients of H_2O and CO_2 (HITRAN96 database). Finally, the resulting spectrum is convolved with the instrumental slit function.

2.3. Comparison of measured and computed spectra

2.3.1. Range 2.4–4.2 μm

The spectrum measured over the range 2.4–4.2 μm (black curve) is compared with the spectral predictions of NEQAIR2-IR (red curve) in Figure 13. As can be seen, all spectral features are well reproduced by the simulations, except between 2.8 and 3.0 μm where the model underpredicts the measurements (possibly because we have not yet incorporated the (3-2) band of OH into NEQAIR2-IR). The contributions of the various radiating systems of importance in this spectral range are shown separately in Figure 14.

It should be noted here that the mole fraction of OH was determined by matching the measured absolute intensities of rotational lines of the P-branch of OH. The OH concentration determined in this manner was then used to infer, using chemical equilibrium relations, the mole fraction of water in the air injected inside the plasma torch. As already mentioned in the introduction, the mole fraction of water injected in the torch was thus found to be approximately 4.5×10^{-3}. This value is significantly lower than the mole fraction of water vapor in room air (0.013). This difference is not surprising as the air injected in the torch was prepared by compressing atmospheric air at an earlier time when the relative humidity may have been lower. Some amount of water vapor may also have been removed by the water trap at the exit of the compressed air tank. Work is in progress to accurately monitor the amount of water vapor injected in the plasma torch during experiments.

Absorption by water vapor in the 6-meter optical path is particularly significant between 2.5 and 2.95 μm, as can be seen in Figure 15 where spectral simulations obtained with and without water absorption are compared with the measured spectrum. This comparison underscores the importance of computing highly accurate positions for all emission and absorption spectral lines, in the present case those of the NO overtone, OH fundamental, and H_2O absorption bands.

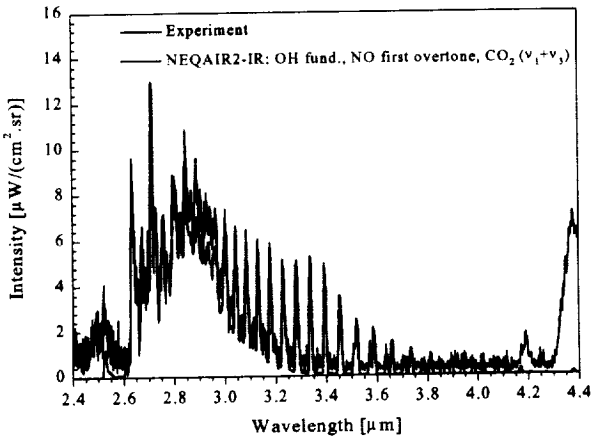

Figure 13. Comparison between measurements and models of infrared emission by air at ~3400 K and 1 atm. The simulations incorporate the effect of water vapor and carbon dioxide absorption over the 6-meter length of room air between the plasma and the detector.

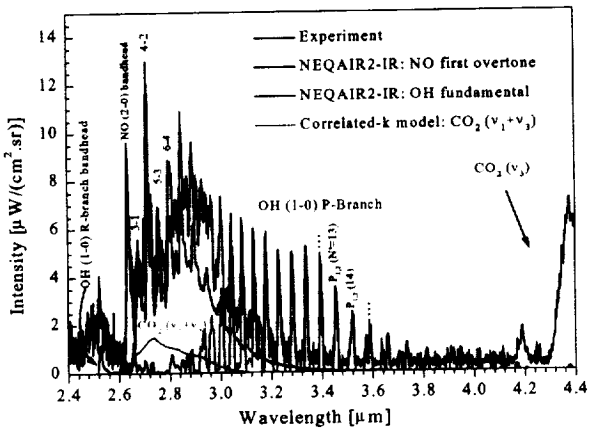

Figure 14. Contributions of NO first overtone, OH fundamental, and CO_2 ($\nu_1+\nu_3$) bands to the total emission spectrum in the range 2.4 – 4.4 μm. Note the abnormally weak OH R branch. These simulations incorporate room air absorption over a 6-meter pathlength.

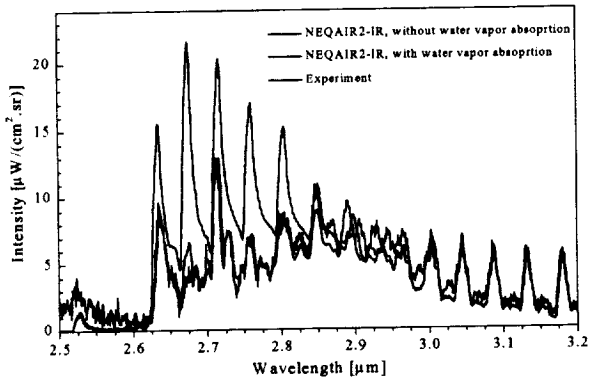

Figure 15. Comparison between the measured emission spectrum and NEQAIR2-IR simulations with and without absorption by water vapor in the optical path.

2.3.2. Range 4.1- 4.9 μm

The measured CO_2 ν_3 band spectrum can be compared in Figure 16 with the predictions of the *correlated-k* model presented earlier. The model also accounts for absorption by room air CO_2 over the optical path separating the plasma from the detector.

This absorption is clearly responsible for near extinction in the range 4.2-4.3 μm of the emission from low-lying rotational levels of CO_2. The lines appearing at both edges of the absorbed region correspond to "hot" CO_2 rotational lines. The model appears to overestimate the measured CO_2 band intensity by approximately 30%. This discrepancy may be due to the fact that the parameters used in the c-k model are only valid at temperatures below 2900 K, which is a temperature slightly lower than the centerline temperature of the plasma considered here (~3400 K). Another possible explanation for the discrepancy may be that the air injected in the torch contained a lower concentration of CO_2 than the typical 330-ppm. However, for the simulation to agree with the measurements, one would have to assume an unreasonably low CO_2 concentration of ~240 ppm. Thus we believe that the intensity differences between the measured and predicted spectra are more likely due to the use of the *c-k* model beyond its range of validity.

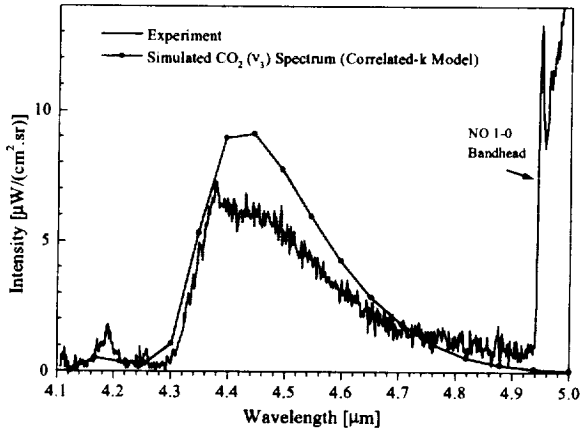

Figure 16. CO_2 spectrum computed with the *c-k* model parameters of the EM2C Laboratory [10, 15], and comparison with the measured spectrum. Note the effects of absorption by room air CO_2 in the range 4.2-4.4 μm.

2.3.3. Range 4.9- 5.6 μm

Figure 17 and Figure 18 compare measurements and modeling results for NO fundamental bands. Two simulated spectra are presented, with and without incorporating the effect of water vapor absorption over the 6-meter path of room air between the plasma and the detector. By matching the depth of the water absorption features in Figure 18, we determined the mole fraction of water vapor in the room to be approximately 0.014. This value is close to the 0.013 mole fraction recorded during the experiment, and within the uncertainties of the measurement.

As can be seen in Figure 18, the predictions of the model (with H_2O absorption) are in excellent agreement with the measured spectrum. It should be noted again that both the measurements and computations are on absolute intensity scales.

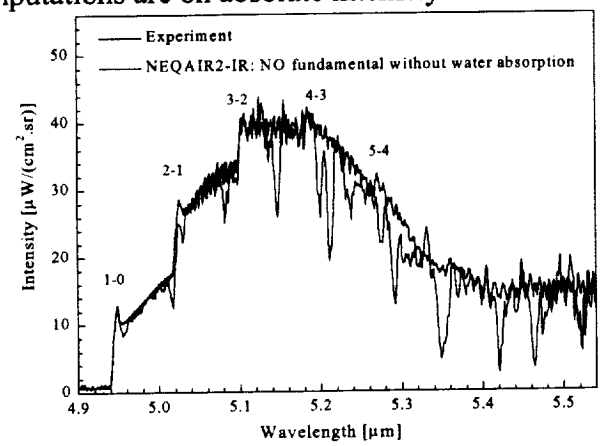

Figure 17. NO fundamental band spectrum computed with NEQAIR2-IR without water vapor absorption, and comparison with experimental spectrum. Note that a (small) constant value of 0.8 μW/(cm².sr) was added to the simulated spectra shown in the figure in order to match the offset, possibly due to underlying continuum radiation, that is apparent at 4.92 μm.

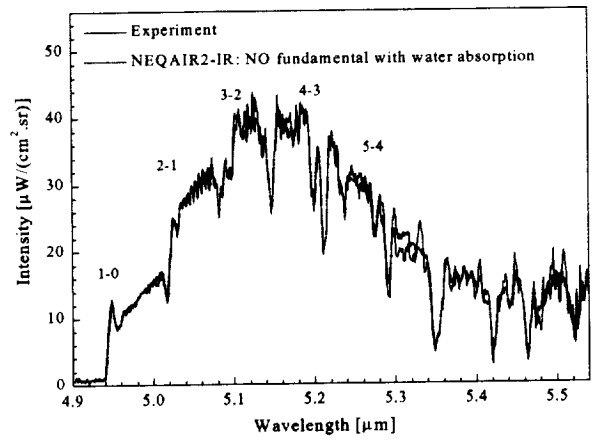

Figure 18. NO fundamental band spectrum computed with NEQAIR2-IR with water vapor absorption, and comparison with experimental spectrum.

2.4. Summary

Detailed absolute intensity infrared measurements and modeling of the spectral emission of atmospheric pressure air plasmas at temperatures up to 3400 K have been made between 2.4 μm and 5.5 μm. The cold gas injected in the plasma torch contained an estimated mole fraction of water vapor of $\sim 4.5\times10^{-3}$ and an estimated carbon dioxide mole fraction of $\sim 3.3\times10^{-4}$. The main emitting systems are the fundamental and overtone bands of NO and OH, and the (ν_3) and ($\nu_1+\nu_3$) bands of CO_2. Special attention was paid to the effects of ambient air absorption in the optical path between the plasma and the detector. As

summarized in Figure 19, excellent absolute intensity agreement is obtained between the measured and simulated spectra of NO emission, CO_2 emission, and room-air CO_2 and H_2O absorption. Very good relative intensity agreement was obtained for OH. Our experimental facility is in the process of being upgraded to allow better monitoring of the humidity of air injected in the plasma torch. This will eventually allow us to test the absolute intensity of the OH model.

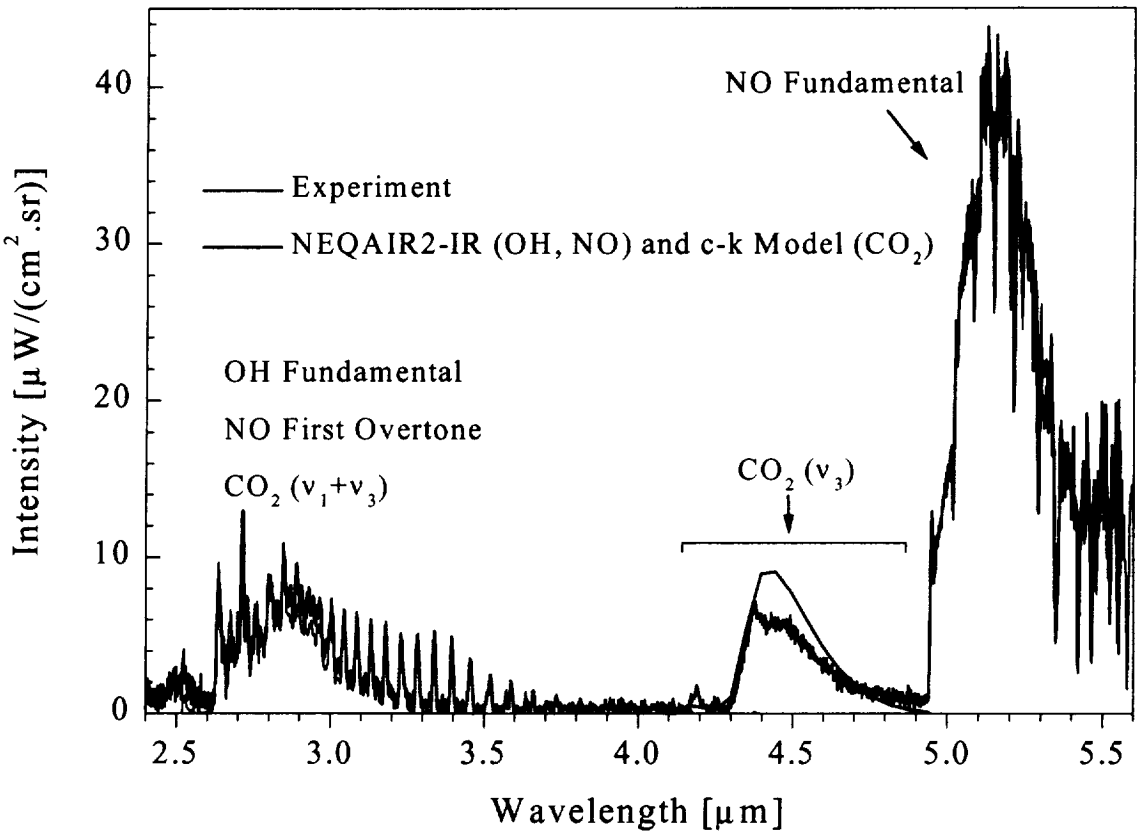

Figure 19. Summary comparison between measurements and models of infrared emission by an air plasma at temperatures of ~3400 K and atmospheric pressure. The simulations incorporate the effect of water vapor and carbon dioxide absorption over the 6-meter length of room air between the plasma and the detector

3. Atomic Lines and Continuum of Air Plasmas in the Infrared

3.1. Introduction

In a previous program (Grant NAG 2-910), spectral measurements were made of the radiation emitted between 1 and 5.5 μm by an atmospheric pressure air plasma in chemical and thermal equilibrium at a temperature of approximately 7,900 K. These measurements [4] revealed the presence of an intense radiation continuum between 3 and 5 μm, a critical spectral range for the detection of infrared missile signatures. The measured continuum was found to be underpredicted by the baseline NEQAIR code, as can be seen in Figure 20 where the simulated continuum only accounts for approximately 25% of the measured continuum. Furthermore, several atomic lines appeared to be missing in the simulations. Sections 3.2-3.5 describe a review of the various continuum processes, as well as suggestions to improve the modeling of continuum radiation. Section 3.6 summarizes results of an effort to improve the modeling of atomic lines in the spectral range 0.8-5 micron. This work was done in collaboration with Dr. Gerhard Hahne from the Computational Chemistry Group of NASA-Ames Research Center. Hahne calculated transition probabilities for transitions NI 4d-5f, 5d-4f, and 4f-5g, which our previous work had shown to be potentially the missing transitions in the range 3-8-4.2 micron

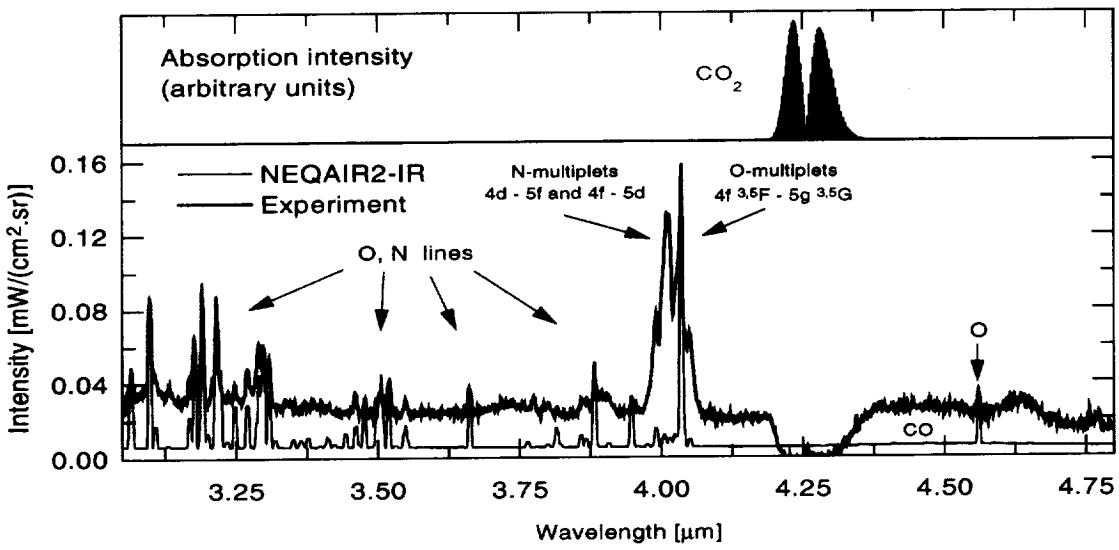

Figure 20. Bottom: Measurements and simulations[4] between 3.0 and 4.8 μm.
Top: Absorption spectrum of CO_2 at 273 K.

Continuum radiation results from the interaction between two particles of which at least one is charged. The interaction produces radiation only if the two particles have different charges in the dipole approximation (quadrupole emission is usually negligible). Therefore e–e, e–A^-, A^-–A^-, A^+–A^+ interactions (where A is any neutral species) do not radiate. It is generally sufficient to consider the interaction between electrons and heavy

particles because the deviation, and hence the emission, of ions is much smaller (~1/1000) than that of electrons owing to their greater mass. The particles interacting with electrons can be considered fixed before impact since the speed of electrons is usually much higher (~100 times) than that of heavy species. Furthermore, because of the large mass difference, heavy species can be considered immobile during the entire collision. Two main types of interaction exist:

- **Absorption/emission of electrons: free-bound radiation**

Free-bound radiation occurs when an electron is absorbed by an ion or neutral. Bound-free radiation is the reverse process and is accompanied by the emission of electrons. This is calculated by NEQAIR in subroutine BFCONT.

- **Deviation of electron trajectories: free-free radiation**

Radiation is emitted when an electron is accelerated, namely when its trajectory is curved by another particle. This radiation is called "free-free" radiation, or Bremsstrahlung, and accompanies the scattering of electrons. Free-free radiation is computed by NEQAIR in subroutine FFCONT.

In turn, these interactions can be subdivided into four types:

- free-free with ions: $e+A^+ \rightarrow e+A^++h\nu$
- free-free with neutrals: $e+A \rightarrow e+A+h\nu$
- free-bound with ions: $e+A^+ \rightarrow A+h\nu$
- free-bound with neutrals: $e+A \rightarrow A^-+h\nu$

Because the continuum is essentially structureless, it is difficult to separate the contributions of the various species and types of continua. Thus discrepancies often exist between measured and calculated continua. In this section, we describe various forms of continuum radiation, including the free-free and free-bound of neutral and ions, then present an analysis of the causes for the discrepancy between modeled and measured continuum. Preliminary efforts to enhance the free-free continuum modeling of NEQAIR are also discussed.

3.2. Free-free with ions:

3.2.1. Background

The free-free electron-ion interaction takes place in the wide-range coulomb field of the ions, and therefore the strength of the interaction is roughly the same for the ion of any atom or molecule. For the temperature range of the present study ($T < 8000$ K), only positive (singly charged) ions need to be considered since their concentration is always much greater (~100 times) than that of negative ions (see Figure 22). As can be seen from Figure 22, the

dominant ions are: NO^+ below 6000 K, N^+, O^+, NO^+ between 6000 and 9000 K, and N^+, O^+ above 9000 K.

The free-free interaction is theoretically well known because it results from a wide range field which allows quasi-classical-hydrogenic calculations to a good approximation. The equation describing this free-free radiation was derived by Kramers [16] and is called Kramers equation (the free-free with ion is also called Kramers radiation). It gives the absorption coefficient α_i for species i, stimulated emission not included:

$$\alpha_i = \frac{4}{3}\left(\frac{2\pi}{3kT_e m_e}\right)^{\frac{1}{2}} \frac{e^6}{(4\pi\varepsilon_0)^3 h m_e c \upsilon^3} Z^2 n_i n_e \qquad [m^{-1}]$$

$$= 3.68\times10^{-2}\frac{Z^2 n_i n_e}{\sqrt{T_e}\upsilon^3} \qquad [m^{-1}] \qquad (1)$$

where T_e is the electron temperature, n_i the density of species i [m^{-3}], Z the charge of the ion, and υ the frequency.

Several authors have proposed refinements to Kramers equation in the form of corrective factors determined from quantum mechanics:

non-classical correction:

In this case the RHS of Eqn. (1) is multiplied by a factor ξ, called the Biberman factor, which is the Maxwellian average of the so-called Gaunt factor [17].

non-hydrogenic correction:

Peach [18-22] proposed to multiply the RHS of Eqn. (1) by a factor (1+D) that includes the g factor. This correction is the one applied in NEQAIR.

Because Kramers equation is a very good approximation, these factors are usually close to unity, as illustrated in Figure 21 with the spectral correction factor (used in NEQAIR) for atomic nitrogen.

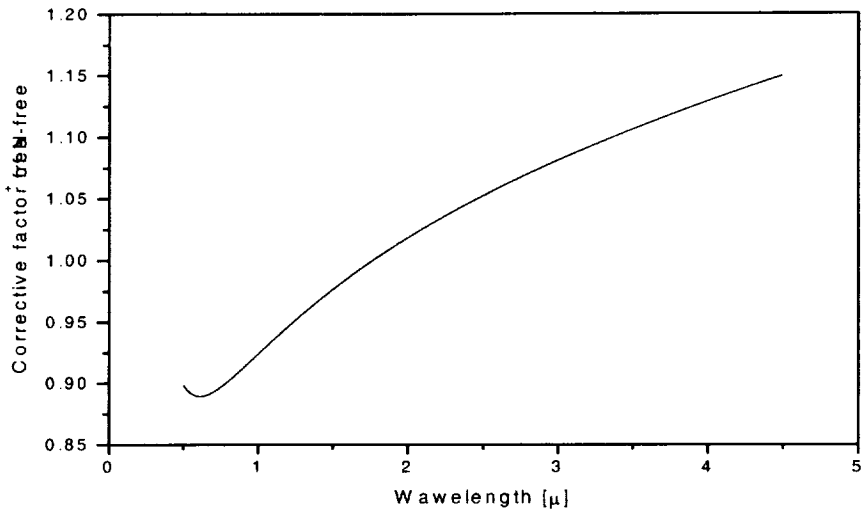

Figure 21. Correction factor for the free-free of N^+ in NEQAIR.

3.2.2. Modifications to the NEQAIR model of ion free-free

The study of subroutines FFCONT and BFCONT brought to light some inaccuracies that we have corrected as detailed below.

1) The NEQAIR routine used to compute the ion free-free is FFCONT. It calculates the correction factor for only two species, N^+ and O^+, because NEQAIR was initially intended for T>10000K where the dominant ions are N^+ and O^+ (see Figure 22). However the dominant ion in the temperature range of interest here (T<8000K) is NO^+ and thus must be included in the calculations. The total ion free-free absorption coefficient can be written as follows:

$$\alpha = \sum_{ions} A(T) n_i g_i = A(T) \sum_{ions} n_i g_i$$

where n_i is the density of ion i, g_i the correction factor for ion i, and (from Eqn.(1)):

$$A(T) = 3.68 \times 10^{-2} \frac{Z^2 n_e}{\sqrt{T} \upsilon^3}.$$

In first approximation we considered g_i=1 for all ions, which is probably a good approximation since free-free correction factors are close to unity. It follows, since the plasma is neutral:

$$\alpha = A(T) \sum_i n_i = A(T) n_e$$

Additional work is required to determine more accurate values for the correction factors of all ions. Nevertheless it can be seen from Table 1 that it is essential to model the free-free due to all ions. The correction has an appreciable effect on the values of the ion free-free continuum computed by NEQAIR for the experimental conditions [4] corresponding to Figure 20.

Table 1. Free-free continuum computed by the baseline NEQAIR and the modified version taking into account all ions.

	Spectral radiance [mW/(cm^2-sr)] at 3.75 μm for our experimental conditions[4] (~8000 K)
Measurement	0.03
Baseline NEQAIR (N^+,O^+ free-free)	0.0058
NEQAIR (all ions free-free)	0.0083

At the temperatures of interest to the missile signature masking problem, the correction is even more important since O^+ and N^+ are negligible. At 6000K, for instance, NO^+ produces over 200 times the radiation of these ions.

2) In NEQAIR, the emission coefficient E_λ is derived using the following relation:

$$E_\lambda = B_\lambda \alpha'_\lambda$$

where α'_λ is the "apparent" absorption coefficient (i.e. including stimulated emission) and B_λ the Planck function. Currently, however, the subroutine FFCONT produces the "true" absorption coefficient (i.e. ignoring stimulated emission) computed with Kramers equation (Zeldovich and Raizer [23], p. 260).

We corrected this error by multiplying α_λ in FFCONT by $1-\exp(-h\nu/kT)$ to obtain α_λ. This correction is not negligible since $h\nu/kT$ is of the order of 1 at our temperature and wavelength conditions. At 3.75 μm and for the conditions of Figure 20, this correction results in the effective decrease of the computed continuum emission coefficient by a factor of 2.5 (Table 2).

The spectrum computed between 3-5 μm with these two corrections is shown in Figure 23.

Table 2. Effect of stimulated emission on the spectral radiance in NEQAIR.

	Spectral radiance [mW/(cm^2-sr)] at 3.75 μm for our experimental conditions[4] (~8000K)
Measurement	0.03
NEQAIR accounting for all ions	0.0083
NEQAIR accounting for all ions and stimulated emission	0.0033

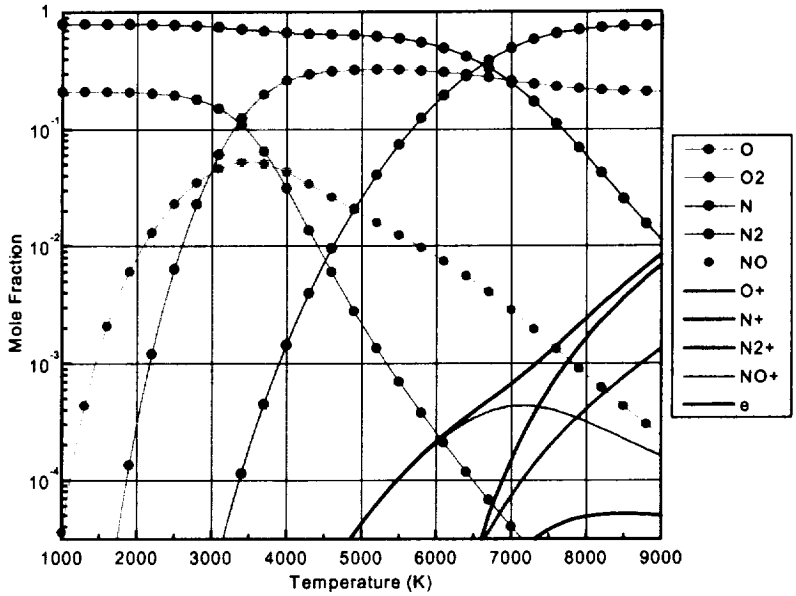

Figure 22. Mole fractions of major species in pure air between 800 and 9000K. At all temperatures, the mole fractions of negative ions remain below 10^{-6}.

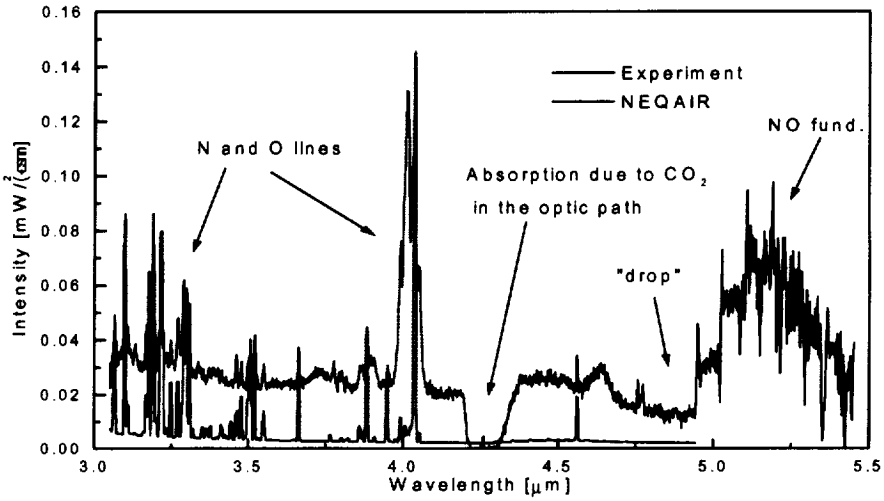

Figure 23. Experimental [4] and computed IR radiation of high temperature air. Continuum computations are limited to the ion free-free.

3.3. Free-free with neutrals

3.3.1. Background

The neutral free-free is due to the interaction of electrons with the electronic orbitals of atoms and molecules. The nature of this interaction is different from the ion free-free, as mentioned by Geltman [24] (p. 601) and John and Williams [25] (p. 169), because unlike electron-ion collisions the electron-neutral interaction occurs at very short range (atomic orbitals).

In air plasmas, the major species interacting with electrons are [N_2, O_2] below 2000 K, [N_2, O, O_2, NO] between 2000 and 5000 K, and [N, O, N_2] for temperatures above 5000 K.

Molecules are expected to have a larger free-free emission cross-section than atoms since the interaction highly depends on the scattering efficiency.

The neutral free-free absorption cross-section is directly related to the elastic electron scattering cross-section [26, 27], or to the momentum transfer cross-section [23, 28]. The relation proposed by Cabannes and Chapelle [26, 27] was recently used in computations of the neutral free-free by Menart et al.[29] and by Wilbers et al.[30]. The electron scattering cross-sections of neutrals are generally one to two orders of magnitude smaller than those of ions. As a result, in highly ionized gases (T > 10,000 K) only the ion free-free is of importance. Below 8000 K, however, it can be seen in Figure 22 that the concentration of neutrals is at least 3 orders of magnitude larger than ions, and therefore their free-free radiation cannot be neglected, contrary to what was done in certain references [17]. Experimental results reported by Taylor [31] (see Figure 24) support the same conclusion. It is thus important to have an accurate description of this continuum.

The neutral free-free has been the object of theoretical and experimental work during the 1960's, in the context of the space program, and theoretical work in recent years. As will be seen below, however, there does not appear to be a consensus on the treatment of electron-neutral interactions.

The models presented in the literature use various approximations: for example, multichannel theory [25], electron scattering or momentum transfer cross-sections [26, 28, 32], atomic potential [24], quantum defect [18, 33], and polarization of the target [34].

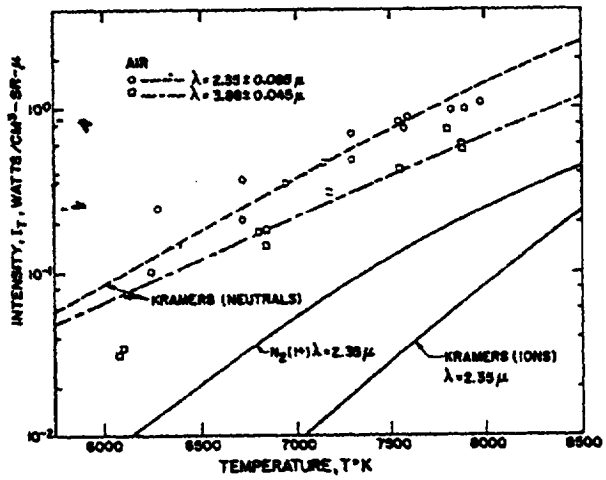

Figure 24. Experimental results [31] showing the relative importance of ion and neutral continua.

Few measurements have been made of the neutral free-free continuum in the temperature and wavelength range of interest for the present work (T<8000K, 1<λ<5μm). With regards to electron scattering cross-sections, accurate measurements [35-37] and calculations [36, 38, 39] have been made for NO, N_2, and O_2. However, there are few measurements and theoretical calculations [40, 41] for O, and only calculations for N [38, 40].

individual species to the neutral continuum, which leads to questionable results as these theoretical expressions may not be accurate. The value of the total neutral free-free radiation is more reliable in these experiments since it is simply obtained by subtracting the relatively well-known ion free-free (Kramers radiation) from the measured continuum.

Evaluation of the intensity of the total continuum itself is further hindered by the presence of superimposed molecular bands. As can be seen in Figure 23 (taken from Ref. [4]), the presence of molecular bands between 3 and 5.5 μm in the measured spectrum may partly contribute to the continuum. The intensity of this molecular emission of unknown origin can be estimated from the drop indicated at 4.8 μm where the real level of the continuum might appear because of the absence of molecular bands.

A review of the cross-sections reported in the literature indicates that large discrepancies exist between calculations and measurements of the free-free continuum. As an illustration, selected values are given in Tables 3-5 of the free-free absorption cross-section Q_{a_i} defined by:

$$\alpha_i = n_e n_{a_i} Q_{a_i} \qquad (Q_{a_i} \text{ in } cm^5)$$

where α_i [cm^{-1}] is the absorption coefficient without stimulated emission and n_i [cm^{-3}] the density of species i.

Table 3. Free-free absorption cross-sections [10^{-38} cm^5]. Sample theoretical and experimental values for Ar and Ne.

Species	T(K)	λ (μm)	Theory Geltman [24]	Experiment Taylor and Caledonia [42, 43]	Experiment Kung and Chang [44]
Ar	9700	3.1	2.5	10	7.5
Ne	12600	3.1	1.8	1.9	6.9
		9.85	52		78

Table 4. Free-free absorption cross-sections [10^{-38} cm^5] for O at ~10,000 K.

λ (μm)	Theory Chung and Lin [34] 10,000 K	Theory Geltman [24] 10,000 K	Theory John and Williams [25] 9700 K	Experiment Taylor and Caledonia [42, 43]	Experiment Kung and Chang [44]
2	0.972	0.713	0. 96		
3.1		2.25 (9700 K)		7.6 (9700 K)	7.8 (9700 K)
3.5	4.63		4.67		
5	12.8	8.97	13.1		
9.85		65.2 (9700 K)			300 (9700 K)
10	96.6	66.8			

Table 5. Calculated free-free absorption cross-sections [10^{-38} cm^5] for O at ~5000 K

λ(μ)	Theory Chung and Lin[34] 5000 K	Theory John and Williams[25] 5040 K
1.14	0.12	0.109
1.52	0.25	0.228
2.28	0.73	0.66
4.56	4.9	4.38

As can be seen from Tables 3-5, discrepancies between computations and measurements often exceed a factor 4. Furthermore, the various models predict different dependence on the temperature for the atomic species. In the case of atomic oxygen for example, the model of Kivel [28] (see Table 8) predicts that the free-free continuum is independent of temperature, contrary to the experimental and theoretical results listed in Tables 4 and 5.

Table 6-7. Temperature and wavelength dependence of semi-empirical free-free cross-sections for O_2 and N_2 (Kivel[32]) [10^{-38} cm^5].

O_2

λ(μm)	6000K	9000K	12,000K
1.2	0.09	0.167	0.26
2.4	0.69	1.3	2.03
4.8	5.33	10.1	16

N_2

λ(μm)	6000K	9000K	12,000K
1.2	0.173	0.36	0.587
2.4	1.28	2.69	4.42
4.8	9.83	20.7	34.3

Table 8-9. Temperature and wavelength dependence of theoretical free-free cross-sections for O and N (Kivel[28]›[32]) [10^{-38} cm^5].

O

λ(μm)	6000K	12,000K
1.2	0.05	0.05
2.4	0.4	0.4
4.8	3.15	3.15

N

λ(μm)	6000K	12,000K
1.2	0.18	0.18
2.4	1.1	1.1
4.8	8	8

Care should be taken with these results since no physical description of the neutral free-free is used to extract these data from experiment, as we already mentioned. For example Taylor [31] and Morris [45] use Kramers equation (Eqn. (1)) for electron-neutral interaction whereas it was derived for electron-ion free-free. They use a Z^2 factor in the equation as a parameter, an "effective charge" determined experimentally, to allow comparison with the electron-ion free-free radiation where Z=1. There is however no theoretical justification for the use of the Z^2 factor (Taylor and Caledonia [42] p. 664). Moreover, while Morris [45] shows over a wide spectral range (0.097 - 0.7 μm) that Z^2

depends on the frequency (Figure 25), Taylor (albeit operating in a shorter spectral range) finds Z^2 to remain approximately constant (Figure 26).

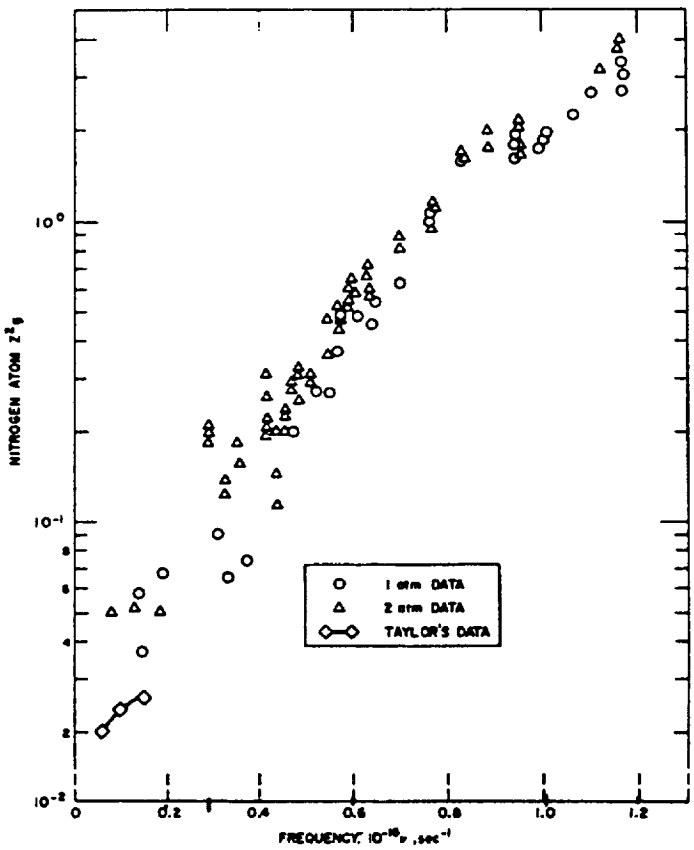

Figure 25. Effective charge factor Z^2 for atomic nitrogen (Morris [45] and Taylor [31]).

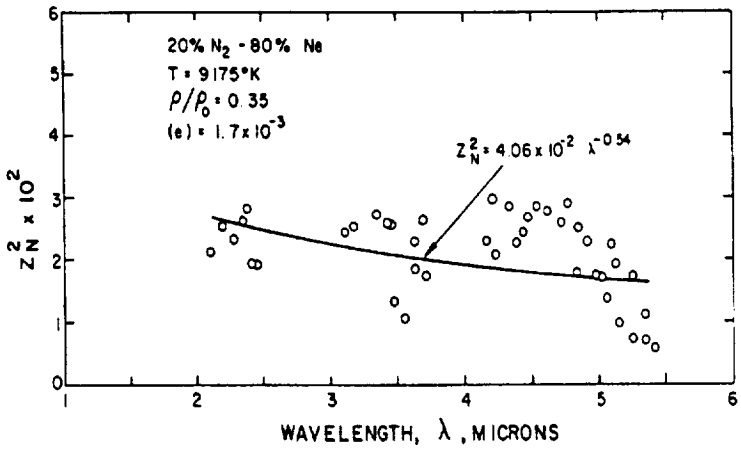

Figure 26. Effective charge factor Z^2 for atomic nitrogen (Taylor and Caledonia [43]).

3.3.2. NEQAIR96 model

Although the free-free continuum of neutrals was not modeled in the original NEQAIR code [46], a model for neutral free-free was incorporated in the recent version NEQAIR96 [47] using equations derived by Peach [19-22]. We suspect however that Peach's equations are not applicable for neutrals for the following reasons.

Peach [18] derived his correction factor explicitly for ions. Then [19-22] this correction factor was applied to the free-free cross-sections of Menzel and Pekeris [48] which are also explicitly for ions (Menzel and Pekeris [48] refer to Nedelsky [49] for electron-neutral interactions). Owing to the very different nature of the electron-neutral and electron-ion interactions, it is unlikely that Peach's results apply for neutrals. We are currently investigating other models [26, 28, 32, 50] and completing a literature search for additional data regarding the neutral free-free continuum.

3.3.3. Estimate of the importance of the neutral free-free

In this section, we analyze the importance of the neutral free-free continuum in the temperature range of interest to the BMDO. Note again that there is no model of the neutral free-free in the original NEQAIR code. The Kivel cross-sections [32] are used for consistency as they are given for the 3 species of interest here, i.e. N, O, and N_2. The comparisons presented below are made at 4.8 μm.

As a first approximation, the plasma is modeled as a 2 cm slab of uniform temperature at 7800 K. This approximation is reasonable since the bulk of the radiation comes from the central part of the plasma which is at a temperature of approximately 7800 K (see Figure 27). We will compare for convenience E_{exp} [W/(cm^2-sr)]/2cm and E_{calc} [W/(cm^3-sr)]. The neutral free-free absorption coefficient without stimulated emission is defined as

$$\alpha_i = n_e n_{a_i} Q_{a_i},$$

where Q_{ai}, n_{ai}, and α_i have dimensions of m^5, m^{-3} and m^{-1}, respectively. The cross-sections are obtained from Kivel [28, 32]. We multiply α_i by $(1-\exp(-h\nu/kT))$ to account for stimulated emission, and by the Planck function:

$$B_\lambda = \frac{2hc^2}{\lambda^5}\left(e^{\frac{h\nu}{kT}} - 1\right)^{-1}$$

to obtain the emission coefficient. The neutral free-free emission coefficient is then defined by the following equation:

$$E_{\lambda,neutral} = \frac{2hc^2}{\lambda^5} e^{-\frac{h\nu}{kT}} \alpha_i \quad \text{[W/(m}^4\text{-sr)]}$$

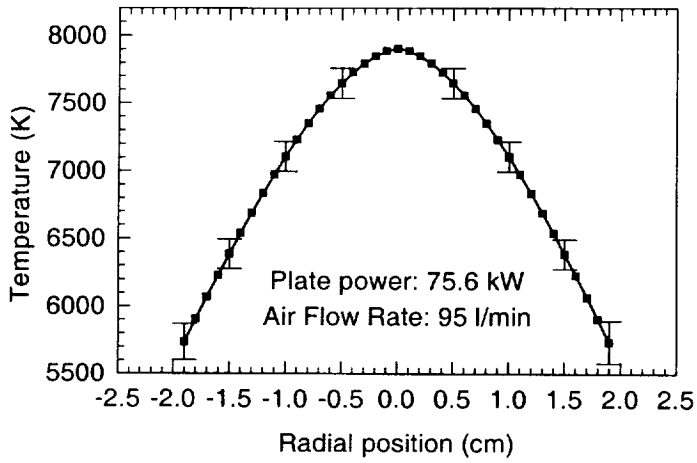

Figure 27. Temperature profile of the plume in experiment of Figure 20.

As the experimental spectrum is convolved with the slit function of the monochromator, we also have to convolve $E_{\lambda,neutral}$ with the same slit function, which has an equivalent width of 0.0065μm. The continuum varies slowly over the equivalent slit width and thus the convolution is simply a multiplication. We finally have:

$$E_{neutrals} = 6.5\times10^{-10} n_e n_a Q_a \frac{2hc^2}{\lambda^5} e^{-\frac{h\upsilon}{kT}} \left[\mathrm{W}/(\mathrm{m}^3 - sr)\right] \quad (2)$$

In turn, the free-free with ions can be determined from Kramers equation (Eqn.(1)) with $n_i=n_e$. The resulting value of α does not take into account stimulated emission, as mentioned in section 2.2.2, so we apply the same correction as for the neutral free-free. We obtain:

$$E_{ions} = 6.5\times10^{-10} \frac{2hc^2}{\lambda^5} e^{-\frac{h\nu}{kT}} \times 3.68\times10^{-2} \frac{Z^2 n_e^{\,2}}{\nu^3\sqrt{T}} \left[\mathrm{W}/(\mathrm{m}^3 - sr)\right] \quad (3)$$

The data used for the present calculations are given in Table 10, and the resulting radiative coefficients are summarized in Table 11. In Table 11, E_i is the free-free emission coefficient and α_i the free-free absorption coefficient of species i.

Table 10. Air composition and neutral free-free cross-sections at T=7800 K and λ=4.8 μm (Kivel [28, 32]).

Species	Air Composition T=7800 K, P=1atm n_a [cm^{-3}]	Free-free Cross-section (Kivel [28, 32]) Q_a [cm^5]	Cross-section per unit volume n_aQ_a [cm^2]
e	1.8×10^{15}		
O	20.3×10^{16}	3.15×10^{-38}	6.4×10^{-21}
N_2	7.23×10^{16}	16.6×10^{-38}	12×10^{-21}
N	62.5×10^{16}	8×10^{-38}	50×10^{-21}

The cross-section per unit volume, n_aQ_a, represents the contribution of each species to the total absorption. We note that N is the dominant neutral for free-free radiation at 7800 K.

Table 11. Calculated radiative coefficients for neutral and ions compared to measured continuum.

	E_i [10^{-7} W/(cm^3sr)]	α_i [10^{-5} cm^{-1}]
O [Eqn. (2)]	2.2	1.15
N_2 [Eqn. (2)]	4.2	2.16
N [Eqn. (2)]	17	9
Total neutral free-free	23.4	12.31
Total ions free-free [Eqn. (3)]	11.4	
Total free-free (neutral + ions)	**34.8**	
Measured continuum at 4.8μm	**60**	

Note: The total ion free-free computed with NEQAIR using the full measured temperature profile of Figure 27 is equal to E_{ions}/2cm=9.5×10^{-7} W/(cm^3-sr). This value is very close to the value of 11.4×10^{-7} W/(cm^3-sr) that we obtained with the assumption of a 2 cm plasma of uniform temperature 7800 K.

Thus, the total estimated free-free emission 34.8×10^{-7} [W/(cm^3sr)] represents approximately half the measured continuum E_{exp}/2cm=60×10^{-7} [W/(cm^3sr)]. The neutral free-free alone represents more than a third of the measured continuum. Uncertainties certainly remain (for instance, Kivel [28, 32] gives Q=4×10^{-39} cm^5 for atomic oxygen whereas John and Williams [25] give Q=10^{-38} cm^5), but nevertheless the neutral free-free appears as a very important emission process in the infrared.

3.4. Free-bound with ions

The ion free-bound continuum is described by the following process

$$A^+ + e \leftrightarrow A^* + h\upsilon ,$$

where A^* represents an electronic state of the neutral species A. The theory is well known for this interaction, and the photoionization cross-sections required for the determination of the emission coefficient have been calculated or measured for many atoms.

The model used in NEQAIR is based on the free-bound Kramers equation with the correction of Peach. As for free-free radiation we corrected the emission coefficient for stimulated emission.

However there are currently two limitations in the NEQAIR model. First, as for the ion free-free, only N^+ and O^+ are taken into account. As already discussed, additional ions must be considered at temperatures below 9000 K. Second, the bound-free radiation stops at 1.4 μm which means that there is a cut-off for the higher energy levels of the atoms. Bound-free absorption from high lying atomic and molecular levels should therefore be considered. We are currently investigating methods to remove these limitations. The starting point will be to incorporate the new bound-free cross sections recently published by The Opacity Project [51].

3.5. Free-bound with neutrals

The neutral free-bound continuum, or attachment, is described by the following process

$$A + e \leftrightarrow A^- + h\upsilon$$

This process is the reverse of the so-called photo-detachment. It is particularly important for electronegative species such as O_2 and O. As several references [45, 52-54] mention the importance of the resulting radiation, further work is required to incorporate this continuum into NEQAIR2-IR.

3.6. Atomic line radiation in the range 0.8-5 micron

This section summarizes the extensions and improvements made to the modeling of atomic line radiation in the infrared range 0.8-5 μm. The atomic radiation database of the original NEQAIR1 code of Park was limited to the transitions listed in the 1966 NBS tables of Wiese et al. [55] that covered the range 0.11-1.26 μm for atomic nitrogen (179 lines) and 0.08-1.32 μm for atomic oxygen (109 lines). In our earlier work [4], the atomic radiation database of the NEQAIR1 code had been augmented by incorporating additional transition probabilities calculated by Biémont and Grevesse[56] and Chung et al.[57], bringing the total number of lines to 548 for atomic nitrogen and 535 for atomic oxygen. These additional lines originate from upper levels between 4p ^{4}S and 6d ^{4}F in the case of nitrogen, and between 4s ^{3}D and 20d ^{3}D for oxygen. As can be seen in Figure 20, with this extended database NEQAIR2-IR reproduced most of the atomic lines measured in the range 3-5 micron. The predicted and measured intensities agree within a factor 2. Yet, there still remain unmodeled atomic lines, particularly around 4 μm. Based on the work of Saum and Benesch [58, 59], it was inferred in Ref. [4] that the missing transitions around 4 μm could be from the 4f–5g multiplet of oxygen and the 4d–5f and 4f–5d of nitrogen. However, no transition probabilities were available at the time to model these transitions. For these reasons, there was still a need to further extend the radiation database of NEQAIR2.

Recently, an updated NIST radiation database was published by Wiese et al. [60] (Electronic version: Atomic Spectra Database (ASD), Martin et al. [61]). This database features 1097 lines of atomic nitrogen in the range 865.23 Å-54.82 μm and 854 lines of atomic oxygen from 697.53 Å to 16.70 μm. This augmented database was incorporated into NEQAIR2. The resulting spectral predictions were found to be similar to those obtained with the earlier database of Biemont and Grevesse. As with Biemont and Grevesse's database, the lines around 4 μm were still not reproduced by the simulations.

To remedy this limitation, Gerhard Hahne from the Computational Chemistry group of NASA Ames Research Center derived a set of transition probabilities for the 4d-5f, 5d-4f, and 4f-5g arrays of atomic nitrogen. Hahne's calculations are based on the experimental energy term values listed by Moore [62], Chang and Sakai [63], and Eriksson [64], and line strength data obtained by deconstructing the theoretical results given by The Opacity Project [51], hereinafter termed TOPbase. TOPbase's results were obtained using only the electrostatic Hamiltonian, and hence all TOPbase levels are characterized by LS (alias Russell-Saunders) coupling. However, significant magnetic/relativistic effects occur in physical nitrogen atoms, in particular when the jumping electron has its initial or final state in a 4f, 5f, or 5g shell. In the 4f and 5f cases, LK-coupling seems to describe the levels best, while in the 5g case, J_cK-coupling seems to be best (these are both intermediate cases between LS- and jj-coupling). It was therefore necessary to take certain weighted averages of

the line strength data in TOPbase to extract estimates for the one-electron radial dipole transition integrals; these results were used to infer estimates for the line strengths in the intermediate coupling schemes. Since S' is not a conserved quantum number in the LK-coupling scheme for the 4f and 5f configurations, Hahne took a weighted average over J, J', and S' of the TOPbase data for the 4d-5f and 5d-4f arrays, and then used the resulting estimates of the radial integrals to obtain line strengths in the LS-L'K' scheme, using Eqns. (9.23) and (14.62) given by Cowan [65]. For the 4f-5g array, Hahne computed line strengths (summed over J and J') from the gA values given by TOPbase using the formulas given by Wiese et al. [60], p.15. Since S is not a conserved quantum number in the LK coupling scheme, and L' and S' are not conserved quantum numbers in the J_c'K' coupling scheme, Hahne took a weighted average over S, L', and S' of the (incomplete—TOPbase does not include L'=5) TOPbase data to obtain estimates for the radial integrals, and then reconstructed the LK-J_c'K' line strengths from these radial integrals using suitable angular momentum coupling coefficients, i.e., Equations (9.24) and (14.63) of Cowan [65]. In this manner, line strengths and positions were determined for the 127 lines of the 4d-5f array, 127 lines of 4f-5d, and 133 lines of 4f-5g.

Saum and Benesch [59], identified lines around 4 μm as belonging to the 4f–5g multiplet of oxygen. To introduce this transition into NEQAIR2, upper state term energies, wavelengths, and Einstein A coefficients were required. The energies of the ^{5}G and ^{3}G terms of the 5g state of oxygen are beyond the range of levels listed in the tables of Moore [62]. Nevertheless, term energies for these states were determined by Chang et al[21] who found them to be nearly degenerate at 105446.226 cm^{-1}. For the 4f ^{3}F and 4f ^{5}F levels, term energies were taken from the ASD database of Ref. [61] as 102968.343 and 102968.249 cm^{-1}, respectively. Thus the 4f ^{3}F-5g^3 G^0 and 4f^{5}F–5g^{5}G^0 transition wavelengths are approximately at 4.0357 and 4.0355 Å, respectively. Since the line separation is much smaller than the experimental slit function of the present experiment (which had a top width of approximately 40 Å), these two multiplets appear as a single line in our experimental spectrum. Einstein A coefficients for this transition were calculated by Chung et al. [57] using single-configuration Hartree-Fock wave functions. They found a *gA* value of 1.149x10^8 s^{-1} for the triplet transition, and 1.916x10^8 s^{-1} for the quintet. The sum of the *gA* value of the triplet and quintet states is therefore 3.065x10^8 s^{-1}. As expected for this high lying 5g state, this value is very close to 4 times the *gA* value of a 5g hydrogenic state, which is itself equal to 1.764x10^7 s^{-1} (TOPbase). The multiplicative factor of 4 corresponds to the ratio of the degeneracy of core oxygen to that of hydrogen (note that the core of H or O does not include nuclear spins, only the electronic core). We also note here that the *gA* values of the 4d^{5}D^0-5f^{5}F and 4d^{3}D^0-5f^{3}F oxygen multiplets obtained from the NIST database are in close agreement with the *gA* values listed inTOPbase (4.4% and 6% larger than the TOPbase values, respectively). These 4d ^{5}D^0-5f ^{5}F and 4d ^{3}D^0-5f ^{3}F oxygen multiplets appear in our experimental spectrum as the two lines at 3.88 and 3.95 micron, respectively.

The spectra calculated with the latest NEQAIR2 database (1097 N lines from NIST database, 127 lines from N 4d-5f, 127 lines from N 4f-5d, 133 lines from N 4f-5g, 854 O lines from NIST database, and 2 lines corresponding to the O 4f-5g multiplets) are shown in Figure 28. The bottom six plots in Figure 28 separately show the contributions of the nitrogen lines of the NIST database, of the 4d-5f, 4f-5g, and 4f-5d N multiplets based on the transition strengths of Hahne, of the O lines of the NIST database, and of the O 4f-5g multiplet determined as discussed in the previous paragraph. Comparison with the measured spectrum (top graph in Figure 28) shows that most of the predicted lines can be found in the experimental spectrum, with the notable exception of several lines belonging to the 4f-5g manifold of atomic nitrogen (see for example that the lines at 4.17 and 4.2 micron in the predicted 4f-5g spectrum do not appear in the experimental spectrum). This discrepancy could be due to inaccuracies in the coupling scheme used to distribute the TOPbase intensities over the 4f-5g multiplet. The N I atomic levels could depart from the assumed LK-coupling in 4f, and from J_c'K' coupling in 5g, to some intermediate case between, say, LS and LK, and LK and J_cK, respectively. Thus more work is required to determine the distribution of line intensities over the 4f-5g multiplet.

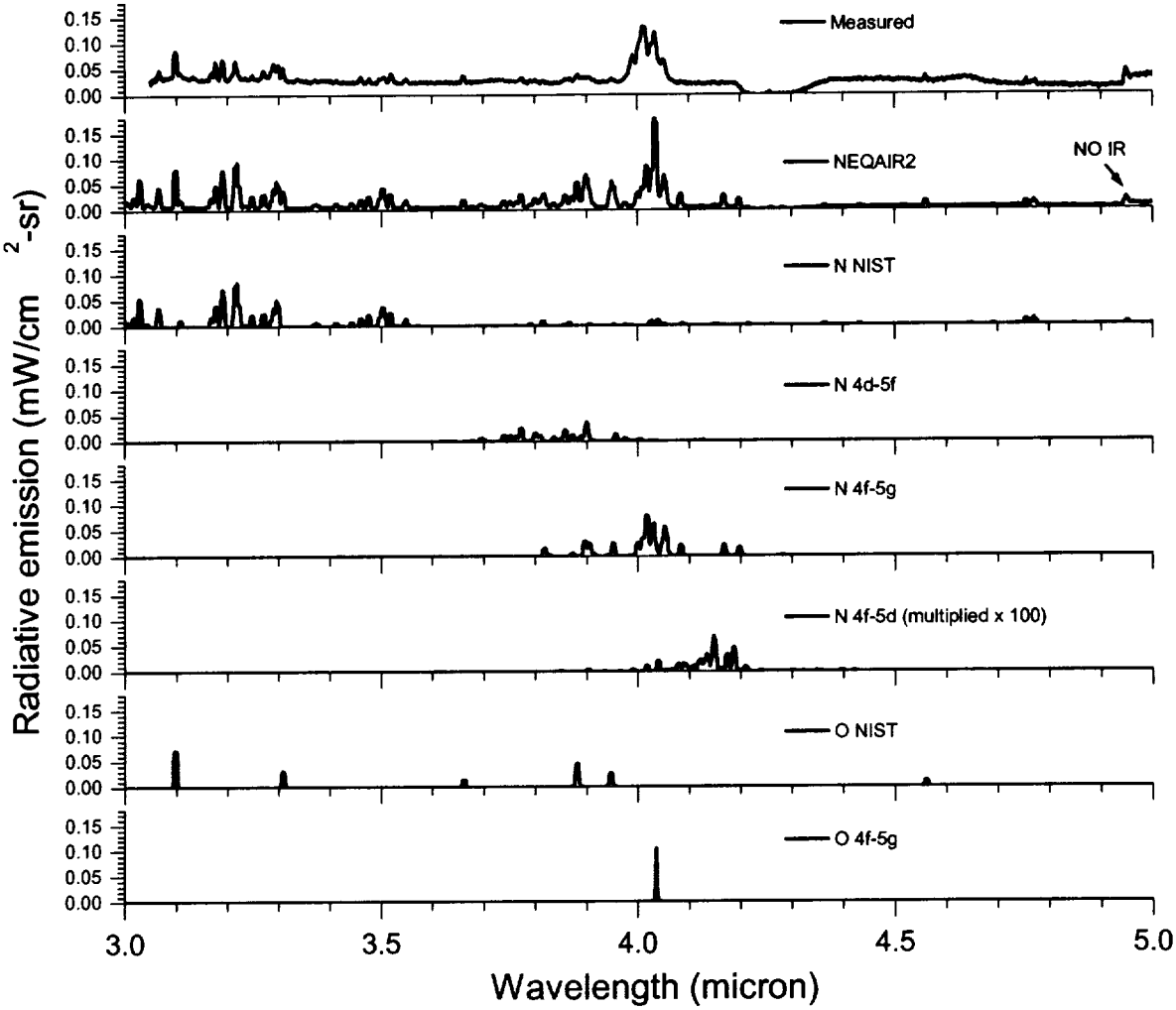

Figure 28. Measured [4] and predicted emission spectra of LTE air for the conditions of Ref. [4] (maximum temperature = 7900 K).

The second observation is that for those lines that seem to appear at correct spectral locations, the predicted intensities are higher than the measurements by a factor of about 1.5 on average. This discrepancy could be due to inaccuracies in the Einstein A coefficients, or to a slight overestimation of the measured temperature profile. To examine this issue, we repeated our spectral calculations with a temperature profile uniformly lowered by 180 K. This difference of 180 K is approximately the error bar of the measured temperature profile (see Figure 4 of Ref. [4]). The spectra computed with this lower temperature profile are shown in Figure 29. It can be seen that all lines from the NIST database, as well as the N 4d-5f and O 4f-5g multiplets, match the measurements satisfactorily with this slightly lowered temperature profile.

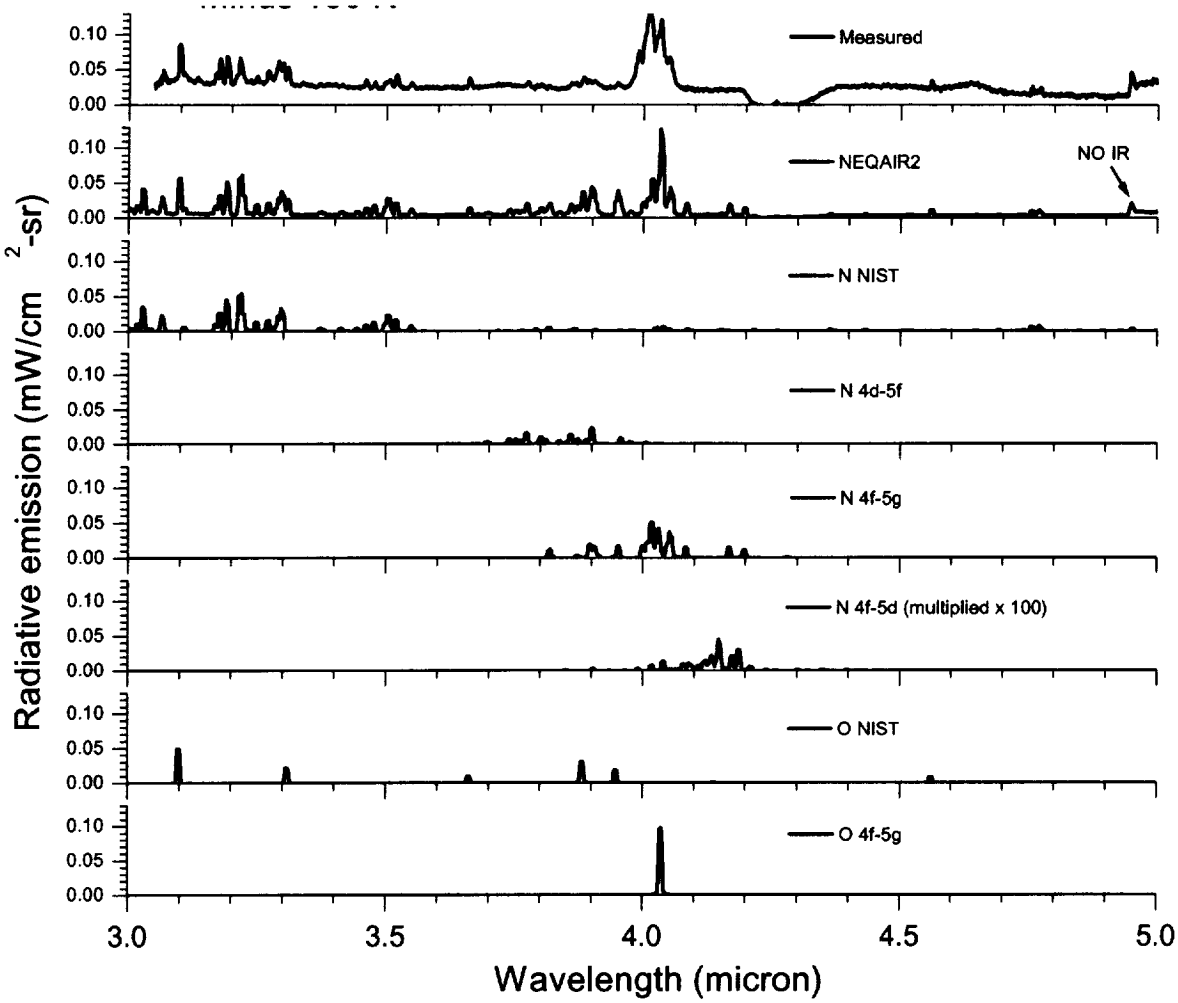

Figure 29. Measured [4] and predicted emission spectra of LTE air with the temperature profile of Ref. [4] uniformly reduced by 180 K (maximum temperature = 7780 K).

In summary, a total of 1484 atomic lines of atomic nitrogen, and 856 lines of atomic oxygen are now incorporated into the NEQAIR2 database of atomic radiation. With the exception of the lines corresponding to the N 4f-5g multiplet, for which a new coupling scheme should be considered, the present spectral predictions of atomic lines are in reasonable agreement with measurements in the range 3-5 micron. Modeling of the underlying continuum remains to be improved, in particular by incorporating the bound-free cross sections determined by The Opacity Project.

Comparisons between spectral predictions and measurements in the range 0.8-3 micron have also been performed to further test and validate the atomic radiation database of NEQAIR2. Results are shown in Figure 30 for 0.8-1.1 micron, Figure 31 for 1.1-1.5 micron, Figure 32 for 1.5-2 micron, and Figure 33 for 3-4 micron. The models used for the various molecular transitions shown in these Figures are described in Ref. [4]. As can be seen from these Figures, the atomic lines predicted with the new atomic radiation database of the present

work are in good agreement with measurements. One notable exception is the region 1.74-1.88 micron of Figure 32 where several experimentally observed lines do not appear in the predicted spectrum. More work is required to identify the missing lines and determine line positions and transition strengths in order to add them to the NEQAIR2 radiation database.

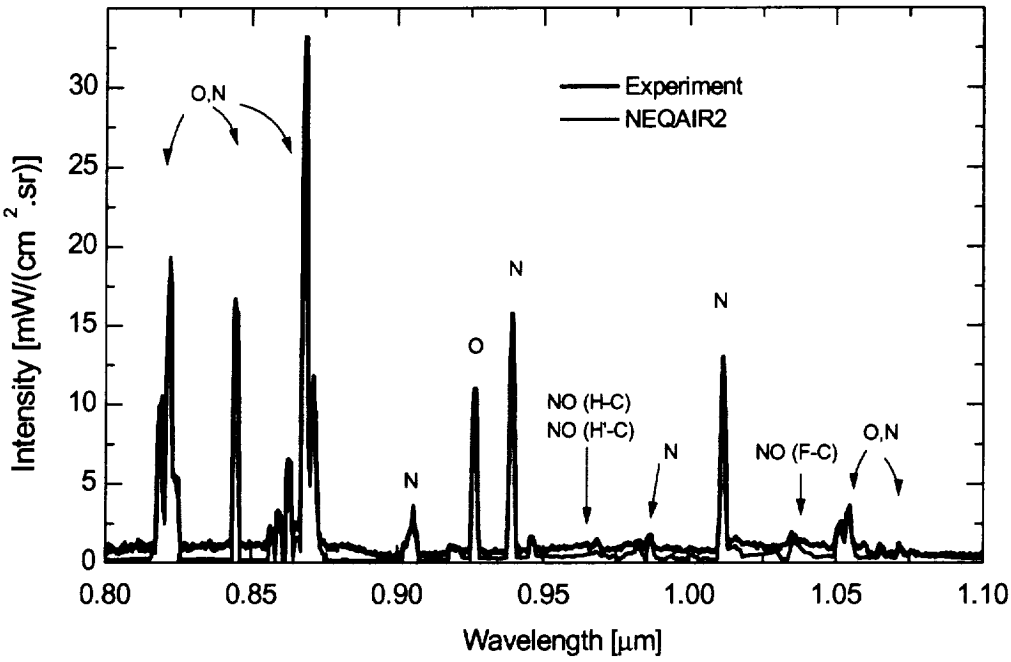

Figure 30. Measured [4] and predicted emission spectra of LTE air with the temperature profile of Ref. [4].

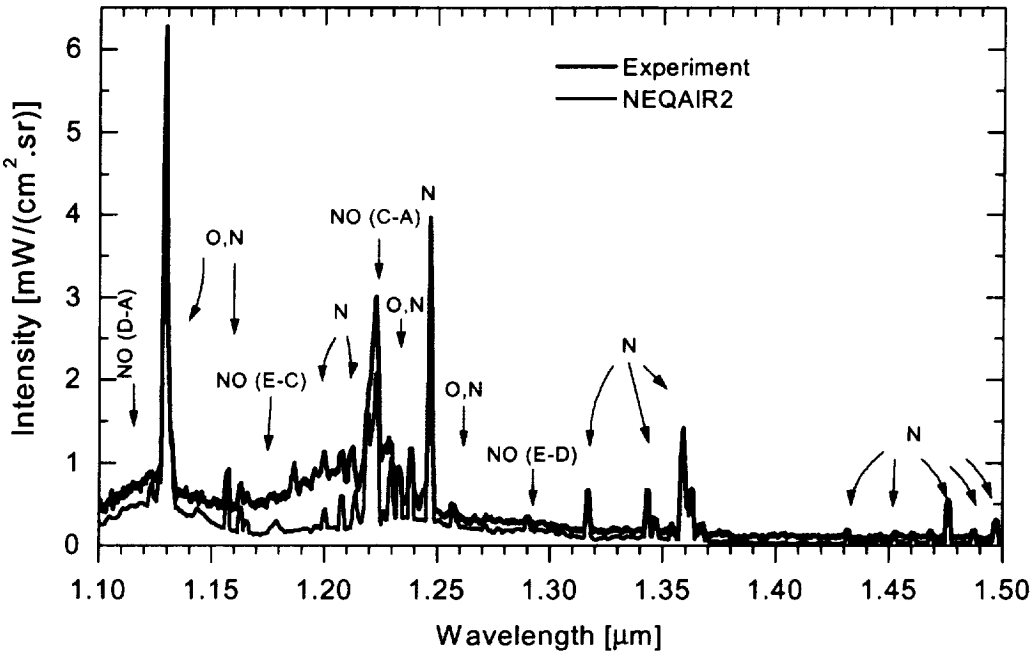

Figure 31. Measured [4] and predicted emission spectra of LTE air with the temperature profile of Ref. [4].

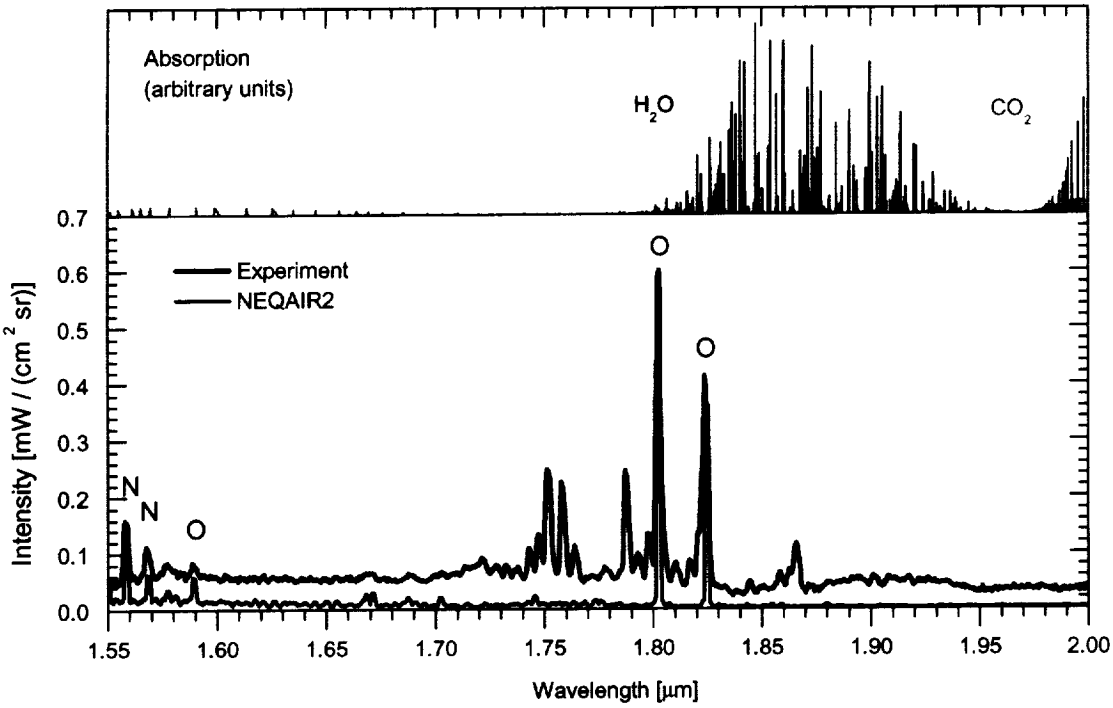

Figure 32. Measured [4] and predicted emission spectra of LTE air with the temperature profile of Ref. [4]. Top frame shows the absorption spectra of the water vapor and carbon dioxide present in the 5-meter room air path between the plasma and the detector.

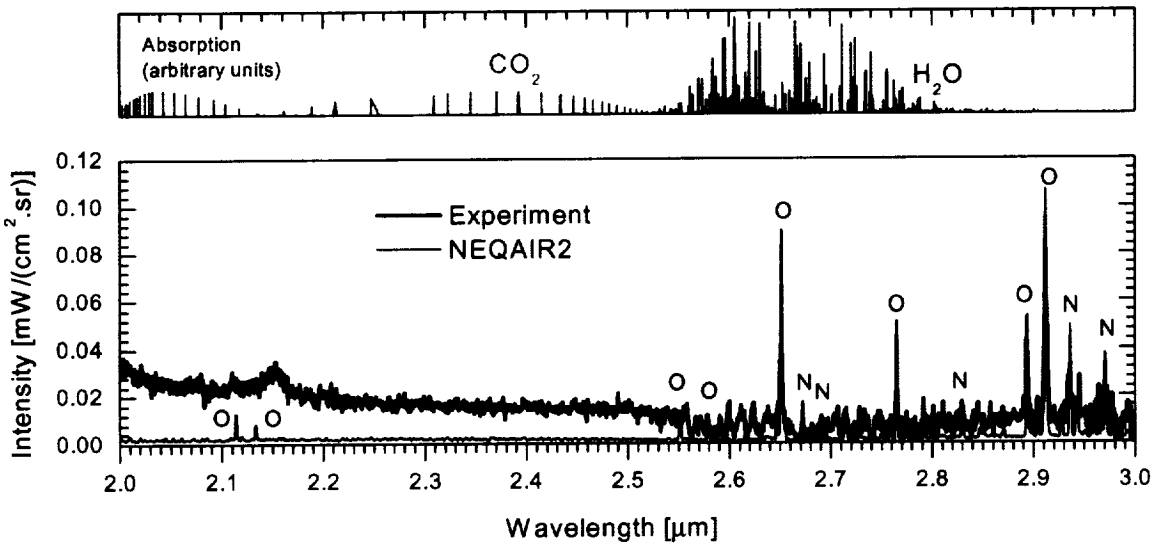

Figure 33. Measured [4] and predicted emission spectra of LTE air with the temperature profile of Ref. [4]. Top frame shows the absorption spectra of the water vapor and carbon dioxide present in the 5-meter room air path between the plasma and the detector.

4. Effects of chemical nonequilibrium on the radiation of nitrogen plasmas

4.1. Introduction

There has been considerable interest in understanding and modeling the chemistry of nonequilibrium molecular plasmas over the past three decades, for applications ranging from atmospheric re-entry to optical diagnostics, material processing, and electromagnetic wave-shielding. Two related but different approaches have been followed toward this goal.

The first is to develop multi-temperature kinetic models [66]. These models consider reactions between different species only, and require that assumptions be made to account for the influence of internal energy levels on the different reactions. They cannot handle nonequilibrium situations in which internal energy levels significantly depart from Boltzmann distributions.

The second is to use collisional-radiative (CR) models, which take into account all significant collisional and radiative mechanisms between the internal energy levels pertaining to the species present in a plasma . Such models are divided in two categories: models that consider transitions between electronic states only [46, 67, 68], and models that consider transitions between vibrational molecular levels [69-71]. No model has been proposed that considers transitions between rotational levels because of the prohibitive computing times required and the lack of accurate knowledge of elementary reaction rates.

The models that consider transitions between electronic states [46, 67, 68] require assuming that vibrational and rotational levels are populated according to Boltzmann distributions at temperatures T_v and T_r, respectively. Therefore, they are unable to account for situations of vibrational nonequilibrium, such as that observed in the recombining N_2 / Ar experiment of Ref. [2]. The vibrationally specific CR models of Refs. [70, 71], on the other hand, can predict departures from vibrational Boltzmann distributions. However, they completely neglect the influence of rotational levels, and crudely account for important reactions such as predissociation.

In a previous publication [69], we presented our first efforts toward the development of a vibrationally specific CR model for nitrogen plasmas that palliates the foregoing deficiencies. In this paper, we present first a new multi-temperature kinetic model based on the same rate coefficient calculation method and the same basic cross-section data as the CR model (Sections 4.2 and 4.3). We detail in Section 4.4 improvements that have been made to the CR model. In Sections 4.5 and 4.6, results of population calculation in nonequilibrium nitrogen plasmas are presented, first in the case of chemical nonequilibrium and thermal equilibrium, and then in the case of thermal nonequilibrium.

4.2. Principles for rate coefficient calculation

In this section, we describe briefly the principles of our method for calculating rate coefficients in plasmas characterized by multiple temperatures. We consider first reactions

between "elementary" energy levels (electronic states for atoms, rovibronic levels for molecules), and then reactions between "grouped" levels, comprised of several elementary levels.

4.2.1. Elementary rate coefficients

The rate coefficient of a binary reaction between two species A and B characterized by Maxwellian velocity distribution functions (VDF's) at temperatures T_A and T_B, respectively, is written:

$$K(\theta)=\frac{8\pi}{\sqrt{\mu}}\frac{1}{(2\pi k\theta)^{3/2}}\int_0^{+\infty}\varepsilon\sigma(\varepsilon)\exp\left(-\frac{\varepsilon}{k\theta}\right)d\varepsilon \tag{4}$$

where $\sigma(\varepsilon)$ is the cross-section of the elementary reaction, μ the reduced mass of A and B, and θ the effective kinetic temperature defined as $\theta = (m_A T_B + m_B T_A) / (m_A + m_B)$, m_i being the mass of species i.

In practice, we assume that electrons have a Maxwellian VDF at temperature T_e and that all heavy species are characterized by Maxwellian VDF's at temperature T_g. Due to the small electron mass m_e, rate coefficients for electron – heavy species reactions are calculated from Eqn. (4) in which μ is replaced with m_e and θ with T_e. For reactions between heavy-species, θ is equal to T_g.

4.2.2. Weighted rate coefficients

The kinetic model considers "chemical" grouped levels, comprised of all internal energy levels of a given species. The CR model considers grouped levels comprised of all rotational levels of a given molecular vibronic level. It is therefore necessary to derive expressions for rate coefficients of reactions involving these grouped levels.

In this report, we employ the Weighted Rate Coefficient (WRC) method detailed in Refs. [72, 73] This method is based on the following formula for the rate coefficient of the reaction $A(l)+M \rightarrow B(u)+M$, where l and u are grouped energy levels of species A and B (atoms or molecules) comprised of several elementary levels i and j, respectively, and M is a colliding partner:

$$K_l^u = \sum_i \frac{[A(i)]}{[A]} \sum_j K_i^j \tag{5}$$

where K_i^j denotes the elementary rate coefficient, $[A(i)]$ the concentration of species A in level i, and $[A]$ the total concentration of species A. Thus, the rate coefficient between grouped levels l and u is equal to a weighted sum over the lower levels i of the summation over the upper levels j of elementary rate coefficients.

If A is a diatomic molecule and l designates the "chemical" grouped level comprised of all rovibronic levels $i = (Y,v,J)$ of molecule A, the ratio $[A(i)]/[A]$ may be written as:

$$\frac{[A(Y,\mathrm{v},J)]}{[A]} = \frac{g_Y(2J+1)}{Q^A_{\mathrm{tot}}(T_{el},T_\mathrm{v},T_r)} \times \exp\left(-\frac{E_Y}{kT_{el}}\right) \times \exp\left[-\frac{G_Y(\mathrm{v})}{kT_\mathrm{v}}\right] \times \exp\left[-\frac{F_{Y\mathrm{v}}(J)}{kT_r}\right] \tag{6}$$

if one assumes that an electronic temperature T_{el}, a vibrational temperature T_v, and a rotational temperature T_r are defined. In the last equation, g_Y denotes the degeneracy of electronic state Y, and E_Y, $G_Y(\mathrm{v})$, and $F_{Y\mathrm{v}}(J)$ stand for the electronic, vibrational, and rotational term energies, respectively. The total partition function of molecule A, $Q^A_{\mathrm{tot}}(T_{el},T_\mathrm{v},T_r)$, is expressed as:

$$Q^A_{tot}(T_{el},T_\mathrm{v},T_r) = \sum_Y g_Y \exp\left(-\frac{E_Y}{kT_{el}}\right) \sum_\mathrm{v} \exp\left[-\frac{G_Y(\mathrm{v})}{kT_\mathrm{v}}\right] \sum_J (2J+1) \exp\left[-\frac{F_{Y\mathrm{v}}(J)}{kT_r}\right] \tag{7}$$

4.3. Kinetic models

In this section, we describe in a first part the widely used multi-temperature kinetic model of Park[66] and in a second part our new kinetic model based on the WRC method for calculating rate coefficients. Comparisons of the WRC results with Park's rate coefficients are given in the following subsections.

4.3.1. Park's model

Park's model [66] is based on the fitting of experimentally determined rate coefficients to formulas of the form

$$K = A\left(\frac{T_x}{10{,}000}\right)^b \exp\left(-\frac{T_d}{T_x}\right) \tag{8}$$

where T_d designates the threshold energy of the reaction under consideration. In a multi-temperature plasma, T_x is either the gas temperature T_g, the electron temperature T_e, or an average temperature T_a expressed as a function of T_g and the vibrational temperature T_v (supposed to be defined) as

$$T_a = (T_\mathrm{v})^q (T_g)^{1-q} \tag{9}$$

where q is a constant whose value lies between 0.3 and 0.5. In practice, we have used the value q = 0.5 for all calculations presented in this report.

Park's rate coefficient parameters relative to nitrogen plasmas are listed in Table 12.

Table 12: Rate coefficient parameters for Park's model (from Ref. [66]).

Reaction	T_x	A (cm^3/s)	b	T_d

$N_2+e \rightarrow N+N+e$	T_a	7.9×10^{-6}	-1.6	113200
$N_2+N \rightarrow N+N+N$	T_a	2.0×10^{-8}	-1.6	113200
$N_2+N_2 \rightarrow N+N+N_2$	T_a	4.6×10^{-9}	-1.6	113200
$N+N \rightarrow N_2^+ + e$	T_g	7.3×10^{-11}	1.5	67500
$N_2+N^+ \rightarrow N_2^+ + N$	T_g	1.7×10^{-10}	0.5	12200
$N+e \rightarrow N^+ + e+e$	T_e	2.2×10^{-5}	-3.82	168200

4.3.2. Present model

The species, energy levels, and reactions taken into account in the present kinetic model are detailed in the following paragraphs. Rate coefficients expressions are given for direct reactions only. Rate coefficients of reverse reactions are calculated by application of the detailed balance principle to elementary cross-sections.

The model is based on the assumption that the internal energy levels of atomic and molecular species are populated according to Boltzmann distributions at temperatures T_{el}, T_v, and T_r. Considering that atomic and molecular electronic states are mainly populated by collisions with electrons and that rotational transitions occur mostly as a result of collisions with heavy particles, we assume further that T_{el} is equal to T_e and that T_r is equal to T_g. The vibrational temperature T_v is a parameter of the model; the two limiting cases $T_v = T_e$ and $T_v = T_g$ will be considered.

In this subsection, we present only rate coefficient calculations in cases where all temperatures are equal, so as to validate the WRC method by comparison with accurate thermal rate coefficients. The influence of different values of T_v when $T_e \neq T_g$ will be illustrated later.

Species and energy levels considered

The different species considered are N, N^+, N_2, N_2^+, and electrons. The internal structure of N is accounted for by using the 22 grouped levels of Park [74], but only ground state N^+ is taken into account. The X, A, B, W, B′, and C electronic states of N_2 and the X, A, and B electronic states of N_2^+ are included, as well as all rovibrational levels belonging to these states.

Electron-impact ionization of N

The total rate coefficient for this reaction is written

$$K(T_e,T_{el}) = \frac{1}{Q_{tot}^N(T_{el})} \sum_Y g_Y \exp\left(-\frac{E_Y}{kT_{el}}\right) K_Y(T_e) \tag{10}$$

where $Q_{tot}^N(T_{el})$ stands for the partition function of atomic nitrogen and $K_Y(T_e)$ designates the rate coefficient of ionization from grouped electronic level Y of N to the ground state of N^+. $K_Y(T_e)$ is calculated from Eqn. (4) using Drawin's ionization cross-section formula [75, 76]:

$$\sigma(\varepsilon) = 4\pi a_0^2 \left(\frac{R_y}{E_Y^{\text{ion}}} \right)^2 \alpha_i \frac{u-1}{u^2} \ln(1.25u) \tag{11}$$

in which E_Y^{ion} designates the ionization energy of electronic state Y and u the reduced impact energy $\varepsilon / E_Y^{\text{ion}}$. The value of α_i was adjusted by matching the value of 10^{-26} cm^6/s measured by Park [77] for the three-body recombination rate at 10,000 K. We found $\alpha_i = 2\times10^{-3}$.

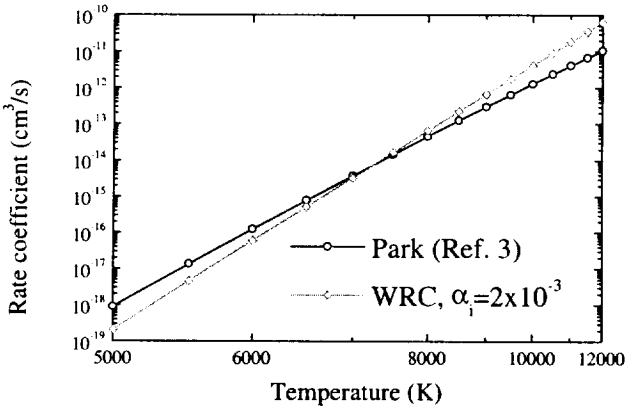

Figure 34. Rate coefficient of electron-impact ionization of atomic nitrogen.

The total ionization rate coefficient calculated with the WRC method and $\alpha_i = 2\times10^{-3}$ is plotted in Figure 34 as a function of temperature T (T_e=T_g=T_v=T) and compared with the value of Park. The two rate coefficients agree within one order of magnitude. The difference in the temperature dependence is due to the value of the exponent in the pre-exponential term of Park's rate coefficient. This value does not come from experimental data but from the theoretical calculations of Bates *et al.*[78]. However, these calculations were performed by means of a collisional-radiative model in an atomic nitrogen plasma, and may not yield results applicable to molecular plasmas.

Electron-impact ionization of N_2

Following Park,[74] we consider that the Franck-Condon principle holds for transitions in molecules caused by collisions with electrons, and that no change in rotational quantum number occurs as a result of such collisions. Therefore, we write the elementary cross-section of ionization from rovibronic level (Y,v,J) of N_2 to rovibronic level (Y',v',J') of N_2^+ as:

$$\sigma(\varepsilon) = q_{Y\text{v}}^{Y'\text{v}'} \delta_J^{J'} \chi\left(\varepsilon, \Delta E_{Y\text{v}J}^{Y'\text{v}'J'}\right) \tag{12}$$

where $q_{Y\text{v}}^{Y'\text{v}'}$ designates the Franck-Condon factor, $\Delta E_{Y\text{v}J}^{Y'\text{v}'J'}$ the ionization energy, and $\delta_J^{J'}$ is equal to 1 if $J = J'$ and to 0 otherwise. We use the binary-encounter-Bethe (BEB) model of Hwang *et al.* [79], which has been shown to yield excellent agreement with experimental cross-sections, in order to calculate the reduced cross-section $\chi(\varepsilon, \Delta E_{Y\text{v}J}^{Y'\text{v}'J'})$.

The total rate coefficient is written:

$$K(T_e,T_{el},T_v,T_r)=\frac{1}{Q_{tot}^{N_2}(T_{el},T_v,T_r)}\times$$
$$\sum_Y g_Y \exp\left(-\frac{E_Y}{kT_{el}}\right)\sum_v \exp\left[-\frac{G_Y(v)}{kT_v}\right] \qquad (13)$$
$$\sum_J (2J+1)\exp\left[-\frac{F_{Yv}(J)}{kT_r}\right]\sum_{Y'}\sum_{v'} K_{YvJ}^{Y'v'J}(T_e)$$

where $Q_{tot}^{N_2}(T_{el},T_v,T_r)$ stands for the total partition function of N_2 and $K_{YvJ}^{Y'v'J}(T_e)$ for the elementary ionization rate coefficient.

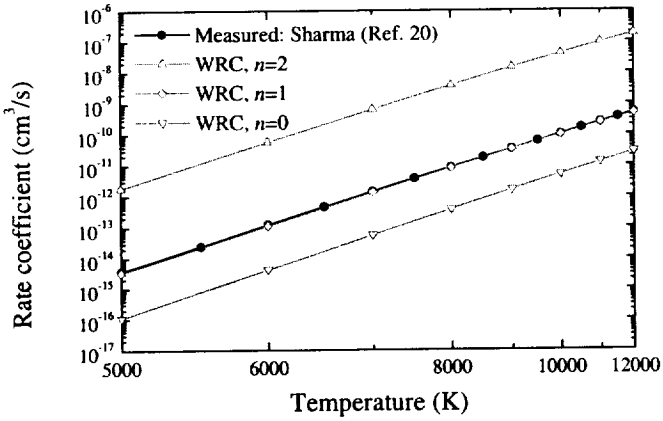

Figure 35. Rate coefficient of electron-impact dissociation of N_2.

Electron and heavy-particle impact dissociation of N_2

By application of the WRC method, the total dissociation cross-section can be written as:

$$\sigma(\varepsilon,T_{el},T_v,T_r)=\frac{1}{Q_{tot}^{N_2}(T_{el},T_v,T_r)}\times$$
$$\sum_Y g_Y \exp\left(-\frac{E_Y}{kT_{el}}\right)\sum_v \exp\left[-\frac{G_Y(v)}{kT_v}\right] \qquad (14)$$
$$\sum_J (2J+1)\exp\left[-\frac{F_{Yv}(J)}{kT_r}\right]\sigma_{YvJ}^{dis}(\varepsilon)$$

where $\sigma_{YvJ}^{dis}(\varepsilon)$ designates the elementary dissociation cross-section. Equation (14) shows that only the ground electronic state of N_2 contributes to the total dissociation cross-section.

Different theoretical [80, 81] or semi-empirical [75] elementary cross-section models suggest that the elementary dissociation cross-section may be written under the general form:

$$\sigma_{YvJ}^{dis}(\varepsilon)=\pi a_0^2\left(\frac{\Delta E_{Y00}^{dis}}{\Delta E_{YvJ}^{dis}}\right)^n \phi_Y(u) \qquad (15)$$

where n is an integer exponent equal to 0, 1, or 2 and $\phi_Y(u)$ a shape function depending only on the electronic state Y. In the last equation, ΔE^{dis}_{YvJ} stands for the dissociation energy of rovibronic level (Y,v,J) and u for the reduced impact energy $\varepsilon/\Delta E^{dis}_{YvJ}$.

With this assumption, Eqn. (14) reduces at low temperature to:

$$\sigma^{dis}(\varepsilon) = \pi a_0^2 \phi_X\left(\varepsilon/\Delta E^{dis}_{X00}\right) \tag{16}$$

Experimental cross-sections are typically measured in a room temperature gas. Thus, in the present model, the elementary dissociation cross-section of rovibrational level (v,J) of N_2 ground state relates to an experimentally determined dissociation cross-section by:

$$\sigma^{dis}_{XvJ}(\varepsilon) = \left(\frac{\Delta E^{dis}_{X00}}{\Delta E^{dis}_{XvJ}}\right)^n \sigma^{exp}\left(\varepsilon \times \frac{\Delta E^{dis}_{X00}}{\Delta E^{dis}_{XvJ}}\right) \tag{17}$$

Neglecting the contribution of excited electronic states, one can write the total dissociation rate coefficient as

$$K(\theta, T_{el}, T_v, T_r) = \frac{g_{N_2(X)}}{Q^{N_2}_{tot}(T_{el}, T_v, T_r)} \times \sum_v \exp\left[-\frac{G_Y(v)}{kT_v}\right] \sum_J (2J+1) \exp\left[-\frac{F_{Yv}(J)}{kT_r}\right] K^{dis}_{YvJ}(\theta) \tag{18}$$

where θ is equal to T_e or T_g, depending on the collision partner.

The rate coefficients of electron-impact dissociation of N_2 calculated with the WRC method from the experimental cross-section of Majeed and Strickland [82] for different values of n are compared in Figure 35 with the rate coefficient determined experimentally by Sharma *et al.*[83]. The present results show the sensitivity to the exponent n. The value $n = 1$ yields excellent agreement with the rate coefficient of Sharma *et al.*

To our knowledge, no experimental data or theoretical model has been published for heavy-particle impact dissociation of N_2. Therefore, we have estimated elementary cross-sections by using Expression (15) and the simple shape function proposed by Park [74]:

$$\sigma^{dis}_{YvJ}(\varepsilon) = \pi a_0^2 \left(\frac{\Delta E^{dis}_{Y00}}{\Delta E^{dis}_{YvJ}}\right)^n \alpha \frac{\ln(u)}{u} \tag{19}$$

where the exponent n is chosen equal to 1, since this value is the most appropriate for electron-impact dissociation.

In Figure 36 are plotted rate coefficients of heavy-particle-impact dissociation of N_2. The WRC values calculated from Eqns. (18) and (19). with $\alpha = 1$ and $\alpha = 0.3$ for collisions with N and N_2, respectively, are in excellent agreement with Park's values.

Dissociative recombination of N_2^+

Similar to dissociation, we write the elementary cross-section for this process as

$$\sigma^{dr}_{YvJ}(\varepsilon) = \pi a_0^2 \left(\frac{\Delta E^{dr}_{Y00}}{\Delta E^{dr}_{YvJ}}\right)^n \phi_Y(u) \tag{20}$$

where $\Delta E^{\mathrm{dr}}_{\gamma \mathrm{v}J}$ designates the (negative) dissociative recombination threshold energy and u the reduced impact energy $\varepsilon / |\Delta E^{\mathrm{dr}}_{\gamma \mathrm{v}J}|$. From the experimental cross-section of Peterson *et al* [84], we have inferred the expression $\phi_X(u) = 0.66/u$ for the shape function of the ground state of N_2^+.

Neglecting the influence of excited electronic states of N_2^+, one gets an expression for the total dissociative recombination rate coefficient similar to Eqn. (18):

$$K^{\mathrm{dr}}(T_g, T_{el}, T_{\mathrm{v}}, T_r) = \frac{g_{N_2^+(X)}}{Q_{\mathrm{tot}}^{N_2^+}(T_{el}, T_{\mathrm{v}}, T_r)} \times \sum_{\mathrm{v}} \exp\left[-\frac{G_\gamma(\mathrm{v})}{kT_{\mathrm{v}}}\right] \sum_J (2J+1) \exp\left[-\frac{F_{\gamma \mathrm{v}}(J)}{kT_r}\right] K^{\mathrm{dr}}_{\gamma \mathrm{v}J}(T_g) \tag{21}$$

where $K^{\mathrm{dr}}_{\gamma \mathrm{v}J}(T_g)$ stands for the elementary dissociative recombination rate coefficient.

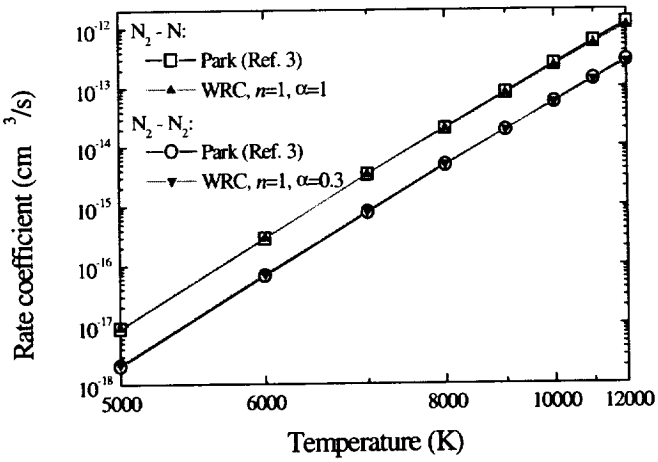

Figure 36. Rate coefficient of dissociation of N_2 by N and N_2 impact.

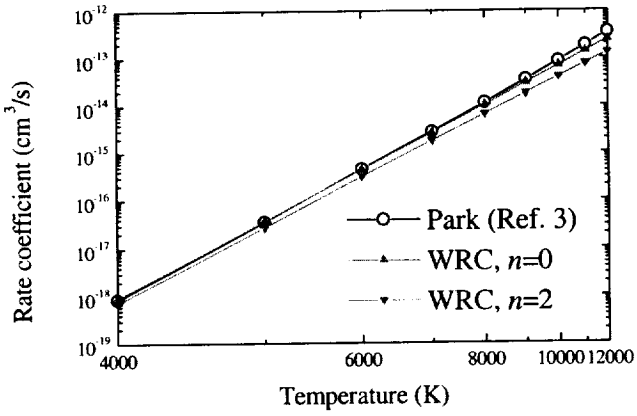

Figure 37. Rate coefficient of the associative ionization $N + N \rightarrow N_2^+ + e$ reaction.

In Figure 37, rate coefficients for the reverse reaction (associative ionization) calculated with the WRC method and different values of n are compared with Park's values. In this case, the WRC results are relatively insensitive to the value of n. The best agreement with Park's rate coefficients is obtained for $n = 0$.

Charge exchange

We consider the charge exchange reaction $N_2+N^+ \rightarrow N_2^+ + N$. This reaction is difficult to account for in a kinetic or a CR model for two main reasons. First, there is a lack of theoretical knowledge of elementary cross-sections. Second, the number of different internal energy levels to consider is very large.

In order to keep the calculation of rate coefficients tractable, we make two simplifying assumptions:

- Only the ground electronic states of N, N^+, N_2, and N_2^+ are concerned by the charge-exchange reaction.
- The elementary cross-section for the reaction $N_2(X,v,J)+N^+(X) \leftrightarrow N_2^+(X,v',J')+N(X)$ can be written as:

$$\sigma_{vJ}^{v'J'}(\varepsilon) = \pi a_0^2 \left(\frac{\Delta E_{vJ}^{v'J'}}{\Delta E_{00}^{00}} \right)^n q_{Xv}^{Xv'} \delta_J^{J'} \phi(u) \tag{22}$$

In Eqn. (22), $\Delta E_{vJ}^{v'J'}$ denotes the threshold energy of the charge exchange reaction. Note that $\delta_J^{J'}$ is a crude approximation of the rotational selection factor, since collisions of molecules with heavy species are likely to cause significant changes in rotational quantum number.

With the foregoing approximations, the experimental data of Stebbings *et al.* [85] can be interpreted to yield the following expression for the shape function $\phi(u)$:

$$\phi(u) = \begin{cases} 0 & u < 1 \\ 5.7 \times \dfrac{u-1}{u_0 - 1} & 1 \le u < u_0 \\ 5.7 & u_0 \le u \end{cases} \tag{23}$$

Since it is not possible to estimate the value of u_0 from the data of Stebbings *et al*, it will be adjusted to match available rate coefficient data.

The total rate coefficient expression can finally be written as:

$$K^{ce}(T_g, T_{el}, T_v, T_r) = \frac{g_{N^+(X)} \times g_{N_2(X)}}{Q_{tot}^{N^+}(T_{el}) \times Q_{tot}^{N_2}(T_{el}, T_v, T_r)} \times \sum_v \exp\left[-\frac{G_v(v)}{kT_v} \right] \sum_J (2J+1) \exp\left[-\frac{F_{vv}(J)}{kT_r} \right] \sum_{v'} K_{vJ}^{v'J'}(T_g) \tag{24}$$

where $K_{vJ}^{v'J'}(T_g)$ stands the elementary charge-exchange rate coefficient.

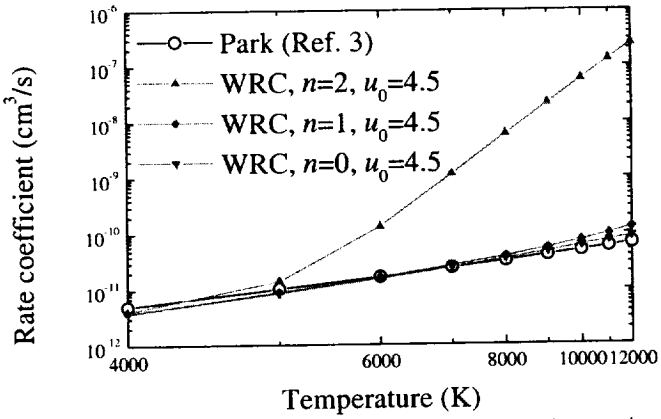

Figure 38. Rate coefficient for the charge exchange $N_2 + N^+ \rightarrow N_2^+ + N$ reaction.

In Figure 39, rate coefficients calculated with the WRC method and different values of n are plotted as a function of temperature. The value $u_0 = 4.5$ was found to yield the best agreement with Park's values. The WRC values, sensitive to the exponent n, are in good agreement with Park's rate coefficients for $n = 0$.

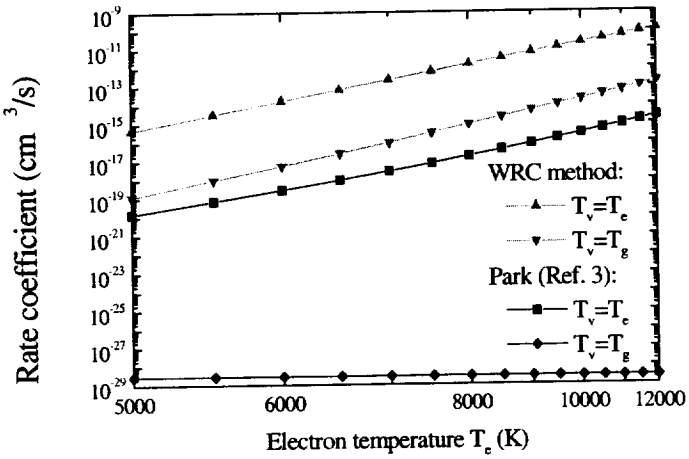

Figure 39. Rate coefficient of electron-impact dissociation of N_2 as a function of T_e, for $T_g = 2000$ K. Two assumptions on T_v are made: $T_v = T_g$ and $T_v = T_e$.

4.3.3. Influence of T_v

We consider in this subsection nitrogen plasmas at a fixed gas temperature $T_g = 2000$ K and an electron temperature T_e different from T_g. We shall use the example of electron-impact dissociation to illustrate the influence of T_v (and more generally of nonequilibrium vibrational distributions) on the foregoing rate coefficients.

In Figure 39 rate coefficients for this reaction are plotted as a function of T_e, as calculated with the WRC method and Park's model [66] using the two assumptions $T_v = T_e$ and $T_v = T_g$. The WRC values are very sensitive to T_v, which is a consequence of the contribution of high-lying vibrational levels to the dissociation reaction. Park's model shows also a large dependence on T_v; however, its predicted rate coefficients are orders of magnitude smaller than those of the WRC model. Indeed, Park's model empirically

combines the contribution of the kinetic temperature (T_e) and the population temperatures (T_{el}, T_v, T_r) through the excitation temperature T_x. By contrast, the present model makes a clear distinction between the contribution of T_e [Eqn. (4)] and the contribution of the population temperatures [Eqn. (18)].

4.4. Vibrationally specific collisional-radiative model

In this section, we describe the CR model used in this study. The species and internal energy levels taken into account are the same as in the kinetic model, but transitions involving electronic states of atoms and vibronic levels of molecules are now considered. The model is essentially the same as that of Ref. [69], with a few additional levels and reactions. Indications of methods used for calculating rate coefficients are only given for direct reactions. As in the kinetic model, rate coefficients corresponding to reverse reactions are calculated from elementary cross-sections obtained by application of the detailed balance principle. The different reactions considered are summarized in Table 13.

4.4.1. Reactions between atomic species

As in the kinetic model, the rate coefficient of electron-impact ionization of electronic state Y of atomic nitrogen is calculated from Drawin's cross-section formula [Eqn. (11)] with $\alpha_i = 2\times10^{-3}$. Rate coefficients for electron-impact excitation of N are those used in the NEQAIR program [46] and listed in Ref. [74].

Radiative emission and absorption are taken into account by means of a radiation escape factor λ. The variation of the number density of level j of atomic nitrogen due to radiative decay to level i is then written as

$$\frac{\partial\left[N(j)\right]}{\partial t} = -\lambda A_i^j\left[N(j)\right] \tag{25}$$

where A_i^j is the Einstein coefficient of the transition. In the present model, we use the A_i^j values of Ref. [46].

Table 13. Reactions considered in the CR model. In the listed reactions, X stands for the ground electronic state of a given species. Y, Y', Z, and Z' are used to refer to any electronic state of atoms and molecules. M stands for any heavy collider (N, N^+, N_2, N_2^+).

Ionization
$N(Z)+e \leftrightarrow N^+(X)+e+e$
$N_2(Y,v)+e \leftrightarrow N_2^+(Y',v')+e+e$
Dissociation
$N_2(X,v)+e \leftrightarrow N(X)+N(X)+e$
$N_2(Y,v)+M \leftrightarrow N(Z)+N(Z')+M$
$N_2^+(Y,v)+M \leftrightarrow N(Z)+N^+(X)+M$
Dissociative recombination
$N_2^+(X,v)+e \leftrightarrow N(X)+N(X)$

Charge exchange
$N_2(X,v)+N^+(X) \leftrightarrow N_2^+(X,v')+N(X)$
Electronic excitation
$N(Z)+e \leftrightarrow N(Z')+e$
$N_2(Y,v)+e \leftrightarrow N_2(Y',v')+e$
$N_2^+(Y,v)+e \leftrightarrow N_2^+(Y',v')+e$
Vibrational excitation
$N_2(X,v)+e \leftrightarrow N_2(X,v')+e$
$N_2(Y,v)+M \leftrightarrow N_2(Y,v')+M$
$N_2^+(Y,v)+M \leftrightarrow N_2^+(Y,v')+M$
$N_2(X,v_1)+N_2(X,v_2) \leftrightarrow N_2(X,v_1-1)+N_2(X,v_2+1)$
$N_2^+(X,v_1)+N_2^+(X,v_2) \leftrightarrow N_2^+(X,v_1-1)+N_2^+(X,v_2+1)$
Predissociation
$N_2(B,12\leq v\leq 18) \leftrightarrow N(X)+N(X)$
$N_2(C,v=4) \leftrightarrow N(X)+N(X)$
Radiation
$N(Y) \leftrightarrow N(Y')+h\nu$
$N_2(Y,v) \leftrightarrow N_2(Y',v')+h\nu$
$N_2^+(Y,v) \leftrightarrow N_2^+(Y',v')+h\nu$

4.4.2. Reactions between molecular species

Reactions included in the kinetic model

All reactions taken into account in the kinetic model are included in the CR model: electron-impact ionization of N and N_2, electron and heavy-particle-impact dissociation of N_2, dissociative recombination of N_2^+, and charge exchange between N_2 and N^+.

In the CR model, rate coefficients for these reactions are calculated with the same methods and the same cross-section data as in the kinetic model, but in which no summation over atomic electronic states is performed and summations over internal molecular levels are limited to rotational levels. Due to the lack of experimental data relative to excited states, this technique is used for atoms and molecules in their ground electronic state only for all foregoing reactions except ionization of N and N_2.

However, heavy-particle-impact dissociation is taken into account for excited electronic states of N_2 in a simplified manner, whereby the last vibrational level below the dissociation limit is assumed to be fully dissociated. Dissociation of other vibrational levels occurs then as a result of VT transfer (see below), mechanism that is sometimes considered as the main dissociation channel. The same method is applied to the calculation of dissociation rates for all electronic states of N_2^+.

The present method is similar to that used by Cacciatore *et al.* [70] and Loureiro and Ferreira [59], with the difference that these authors consider a fictitious dissociating vibrational level just above the dissociation limit. We believe that the two methods yield similar results except for very high-lying levels, and plan to investigate this point in future work.

Electron-impact excitation

Rate coefficients of electron-impact excitation of N_2 and N_2^+ are calculated with the method described in Ref. [69]. For excitation from the ground state of N_2, we use the experimental cross-section data of Cartwright *et al.*[74] For excitation between excited electronic states of N_2 and for all transitions in N_2^+, we use Seaton's model [80] with the Gaunt factor of van Regemorter [75] for optically-allowed transitions, and Drawin's model [75, 76] for optically-forbidden transitions.

Vibrational excitation

Vibrational excitation of N_2 ground state by electron impact (e-V transfer) occurs via resonant transitions to the ground state of the unstable negative ion N_2^-. To our knowledge, no similar mechanism has been reported for excited electronic states of N_2 or for N_2^+. In the CR model, we use the cross-section calculation method of Kazansky and Yelets [86]. This method reproduces available experimental cross-sections corresponding to low-lying vibrational levels within about 10 %, and can be extended in a straightforward manner to higher-lying vibrational levels.

Vibrational excitation by heavy-particle impact (VT transfer) is taken into account for all electronic states of N_2 and N_2^+ and all collision partners (N, N^+, N_2, N_2^+). Rate coefficients for this mechanism are calculated according to the SSH model in the formulation of Billing and Fischer [87]. For N_2 ground state and collisions with N_2, the value of K_1^0 is taken from Ref. [88]. For other electronic states of N_2 or other collision partners, and for all electronic states of N_2^+, the value of K_1^0 is calculated from the general fitting formula given in Ref. [89].

The VV transfer mechanism is included for the ground states of N_2 and N_2^+. (For excited electronic states, VV transfer is negligible with respect to VT transfer.) Rate coefficients are calculated with the SSH model in the formulation of Bogdanov *et al*[90] for N_2 and of Billing and Fischer for N_2^+ [87].

Predissociation

Predissociation is a mechanism by which some vibrational levels of N_2 (B) and N_2 (C) spontaneously decay into two ground state N atoms:

$$N_2(B, 12 \le v \le 18) \leftrightarrow N(X) + N(X) \tag{26}$$

$$N_2(C, v=4) \leftrightarrow N(X) + N(X) \tag{27}$$

This mechanism is caused by the crossing of the stable potential energy curves of the B and C states of N_2 with unstable potential energy curves.

For N_2 (B), we use the method for calculating predissociation rate coefficients based on the experimental data of Geisen *et al.* [91] described in Ref. [69]. Since no data are available for N_2 (C), we use the simple assumption that level $v = 4$ is in equilibrium with ground state N atoms.

Radiation

As for atomic nitrogen, the effect of radiative transitions in N_2 and N_2^+ is taken into account by means of the radiation escape factor λ. For instance, the variation in the number density of vibronic level (Y', v') of N_2 due to a radiative transition to level (Y, v) is written:

$$\frac{\partial\left[N_2(Y', v')\right]}{\partial t} = -\lambda A_{Yv}^{Y'v'}\left[N_2(Y', v')\right] \tag{28}$$

where $A_{Yv}^{Y'v'}$ designates the Einstein coefficient of the transition.

The Einstein coefficients of all radiative transitions considered in the model (B-A, C-B, W-B, B′-B systems of N_2, A-X, B-X systems of N_2^+) have been calculated with the method detailed in Ref. [92].

In the atmospheric pressure plasmas considered in this report, the collision frequencies are such that radiative transitions are a negligible population mechanism, and we have used in practice the value $\lambda = 0$ (optically thick medium) in all presented calculations. However, the CR model is capable of accounting for the effect of radiative transitions at lower pressures.

4.5. Chemical nonequilibrium

In this section, we consider the case of plasmas in thermal equilibrium and chemical nonequilibrium, i.e. in which only one kinetic temperature T is defined ($T_e = T_g = T$) but species are under- or overpopulated with respect to their equilibrium concentration at T. It is convenient to characterize such situations by using overpopulation factors ρ_S defined as:

$$\rho_S = \frac{[S]}{[S]^{eq}} \tag{29}$$

where [S] and $[S]^{eq}$ stand for the actual and equilibrium (at temperature T) number density of species or energy level S, respectively. For instance, dissociation equilibrium between N_2 and N atoms is simply written in this formalism as $\rho_{N2} = \rho_N \times \rho_N$.

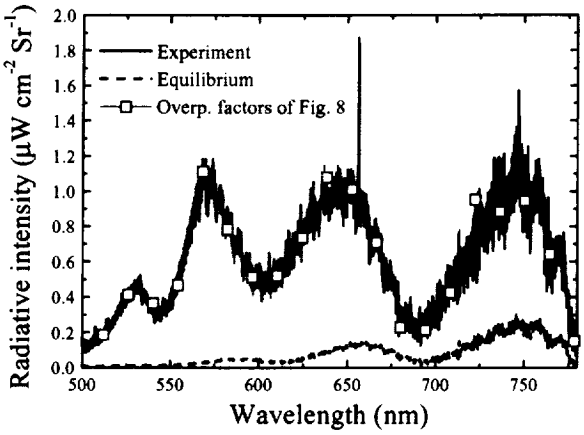

Figure 40. Radiative intensity emitted by the N_2 B-A system, as measured by Gessman *et al.* [2] and calculated under equilibrium at 4720 K and with the "experimental" overpopulation factors of Figure 41

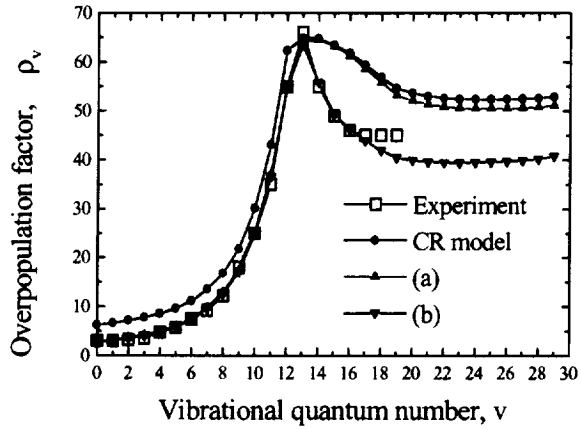

Figure 41. Vibrational overpopulation factors of the N_2 B state. CR model calculation performed with $T = 4720$ K, $p = 1$ atm, $n_e = 7.3\times10^{-3}$, $\rho_N = 8.1$. (a): CR model with N_2 (X-A) and N_2 (X-B) electron-impact excitation rates multiplied by 4 and the N_2 (B,v=12) predissociation rate divided by 5. (b): same as (a) without predissociation of levels $v \geq 14$ of N_2 (B).

We shall focus on comparing predictions of the CR model with some of the experimental results of Gessman *et al.*[2], who performed detailed measurements of species concentrations in a recombining nitrogen / argon plasma. In these experiments, a mixture of ~100 slpm N_2, ~50 slpm argon, and ~2.3 slpm H_2 was inductively heated with a 50 kW RF plasma torch. The plasma produced in this manner was accelerated to a velocity of ~1 km/s by passing through a 1 cm diameter nozzle, and then rapidly cooled (within ~250 μs) in a 15 cm-long water-cooled modular brass test-section. Although the plasma was found to remain always close to thermal equilibrium, chemical nonequilibrium was observed at a location 5 mm downstream of the 15 cm test-section, with a centerline temperature of ~4720 K.

In Figure 40 is plotted the radiative intensity emitted by the first positive (B-A) system of N_2, as measured by Gessman *et al.* [2]. The departure from the equilibrium spectrum (calculated with the NEQAIR2 code [46, 93]) shows that the emitting electronic state (B state)

is overpopulated. The population of the vibrational levels of the N_2 B state can be determined by trying to match the emission spectrum predicted by NEQAIR2 and the measured spectrum. Remarkable agreement is obtained by using the "experimental" overpopulation factors of Figure 41. (Note that these overpopulation factors were recently recalculated [94] using an improved radiation model and are slightly different from those of Ref. [2].)

Argon is not included in the CR model, but it is likely that reactions with argon do not significantly affect the population of the N_2 B state. We shall therefore try to reproduce Gessman's results in a pure nitrogen plasma in chemical nonequilibrium. The CR model calculations are in this case performed by making use of the quasi-steady-state (QSS) approximation, in which all excited levels of atoms and molecules are supposed to be in steady-state, and equations relative to ground levels are replaced with mass conservation equations.

The input parameters of the model are the temperature $T = 4720$ K, the pressure $p = 1$ atm, and the concentrations of the different species, listed in Table 14. The electron number density is the same as in Gessman's experiment. The N atom overpopulation factor has been calculated by assuming that the vibrational level v = 13 of the B state is fully coupled with ground state N atoms via predissociation, as suggested in Ref. [57]: $\rho_N = [\rho_{N2(B,v=13)}]^{1/2} \approx 8.1$. The concentrations of N^+ and N_2^+, which have little influence on the N_2 B state population, have been chosen in such a way that the plasma is electrically neutral and that the charge exchange reaction $N_2+N^+ \leftrightarrow N_2^++N$ is balanced.

The vibrational overpopulation factors determined by Gessman *et al.* [2, 84] are plotted in Figure 41 together with three calculation results of the CR model with different values of a few controlling rates. The curve labeled "CR model" was obtained using the rate coefficients of Section 4.4. It reproduces the general shape of the experimental curve, with a peak at v = 13, but predicts larger overpopulation factors at both small and large v's.

Table 14. Species concentrations used to simulate the experiment of Gessman et al.

S	$[S]^{eq}$ (cm^{-3})	[S] (cm^{-3})	ρ_s
N	1.5×10^{17}	3.8×10^{13}	8.1
N^+	4.8×10^{10}	3.8×10^{13}	~800
N_2	1.5×10^{18}	1.5×10^{18}	~1
N_2^+	3.5×10^{11}	3.5×10^{13}	100
e	4.0×10^{11}	7.3×10^{13}	180

We have attempted to obtain better agreement with Gessman's measurements by varying a few controlling rates. Curve (a) was calculated by multiplying the N_2 (X-A) and N_2 (X-B) excitation and de-excitation rates by a factor of 4, and by dividing the predissociation rate of level N_2 (B,v = 12) by a factor of 5. Note that, for lack of available experimental data, the value of the N_2 (B,v = 12) predissociation rate used in the CR model is no more than an estimate based on the value measured by Geisen *et al.* [91] for v = 13, so that

the foregoing adjustment to the rate is reasonable. Similarly, the multiplicative factor of 4 for the X-A and X-B excitation rates is not unreasonable, given the uncertainty on cross-sections for these reactions.[95] With these modified rates, excellent agreement is obtained with the experimental curve, except for values of v greater than 14, for which the overpopulation factors seem to be too large. This suggests that, in the model, the coupling with N atoms due to predissociation may be too strong.

Curve (b) presents a limiting case, in which the rates are modified as in curve (a) and predissociation of levels $v \geq 14$ is neglected. Excellent agreement with the experimental curve is now shown for high-lying levels. This result supports the fact that predissociation rates for levels $v \geq 14$ may be overestimated in the model, but does not mean that these levels do not predissociate. The discrepancy between curve (a) and the experimental curve may indeed come from uncertainties on other rates (VT transfer, for instance). Moreover, the experimental uncertainty on the overpopulation factors of high-lying levels remains quite large (on the order of ± 10), because these levels contribute little to the total emission of the first positive system of N_2 [94].

Figure 42 shows the vibrational overpopulation factors of the X, A, B, W, B′, and C states of N_2 as a function of the vibrational quantum number v, calculated with the same modified rates as curve (a) of Figure 41. All states have overpopulation factors of low-lying levels in the range 2 to 4, which indicates that they are in partial equilibrium with each other. The overpopulation factor of the X, A, and C states increase steadily with v to reach values close to that corresponding to dissociation equilibrium. The W state overpopulation curve exhibits two inflexion points, and the B′ state overpopulation curve has a local maximum similar to that of the B state. These behaviors are caused by collisional coupling with predissociating levels of the B state.

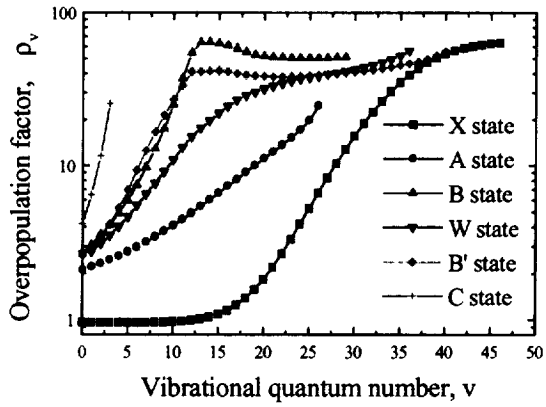

Figure 42. Vibrational overpopulation factors of the X, A, B, W, B′ and C states of N_2. Same conditions as curve (a) of Figure 41.

4.6. Thermal nonequilibrium

In this section, we consider the case of nitrogen plasmas in thermal nonequilibrium, in which the electron temperature T_e and the heavy-species temperature T_g are different. We compare predictions of the CR model with those of Park's and the present kinetic models for steady-state plasma compositions. We shall focus on the evolution of the electron number density as a function of the electron temperature. Generating "cold" molecular plasmas with an elevated electron number density is indeed of interest in applications ranging from material processing to electromagnetic wave shielding.

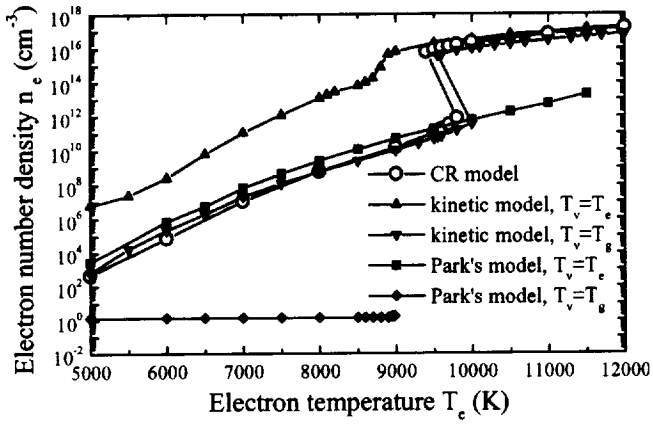

Figure 43. Electron number density as a function of T_e in an atmospheric pressure nitrogen plasma at T_g = 2000 K.

Figure 43 shows the steady-state electron number density n_e as a function of T_e in an atmospheric pressure nitrogen plasma at T_g = 2000 K, as calculated with the CR model and the two kinetic models with two different assumptions on T_v. Note that the N_2 (X-A) and N_2 (X-B) excitation and N_2 B predissociation reactions have little influence on the electron number density; in practice, the rate coefficients of these reactions used in the CR model for the present calculations are those predicted by the method of Section 4.4 and not the modified values suggested in Section 4.5. Steady-state solutions are obtained either with the CHEMKIN program [96] modified to handle two-temperature chemistry (kinetic models) or by using directly the differential equation solver LSODE of CHEMKIN (CR model).

The solution obtained with the CR model is considered as a reference, since no assumption on the value of T_v is required. Figure 43 shows a steady increase in n_e with T_e up to 9800 K, and then an S-shaped jump to larger values of n_e, after which n_e continues to slowly increase with T_e. This behavior is due to a large extent to electron-impact dissociation of N_2, the rate coefficient of which increases with T_e. Before the jump, this reaction is balanced by inverse dissociation by heavy-particle (N_2 or N) impact. The jump occurs when T_e is so high that electron-impact dissociation cannot be balanced any more: the number density of N atom increases, and consequently the number density of N^+ and of the electrons,

because of electron-impact ionization of N. A limit is reached after the jump, when N_2 is almost fully dissociated.

The electron number density values predicted by the present kinetic model are very sensitive to the assumption made on T_v: $T_v = T_g$ yields excellent agreement with the CR values at low electron temperatures, while $T_v = T_e$ seems more appropriate at high electron temperatures. This suggests that a transition takes place between a regime where vibrational levels are equilibrated mainly by collisions with heavy particles and a regime where they are equilibrated by collisions with electrons. The electron number densities predicted by Park's kinetic model [66] are also very sensitive to the assumption on T_v. However, they depart significantly from the CR values. In particular, the S-shaped behavior is not reproduced. The discrepancies can be traced to the incorrect dependence of Park's rate coefficients on the various temperatures.

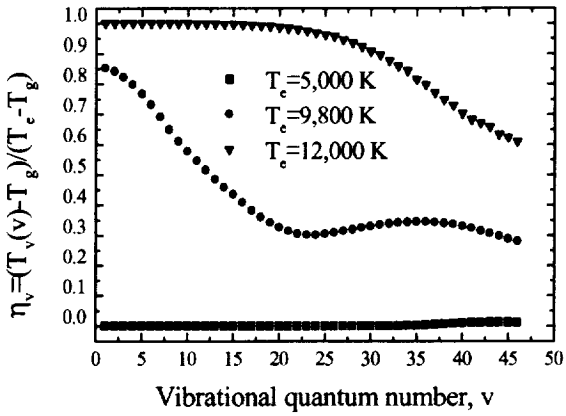

Figure 44. Relative difference $\eta_v=(T_v(v)-T_g)/(T_e-T_g)$ as a function of the vibrational quantum number v of the ground state of N_2 for three values of T_e, in an atmospheric pressure nitrogen plasma at T_g =2000 K.

In order to provide additional insight on the vibrational temperature value, we have plotted in Figure 44 the quantity $\eta_v=(T_v(v)-T_g)/(T_e-T_g)$ as a function of the vibrational quantum number. $T_v(v)$ is defined as the effective vibrational temperature of vibronic level (X,v) of N_2 with respect to the ground state:

$$T_v(v) = \frac{1}{k} \times \left[G_X(v) - G_X(v=0) \right] / \ln\left(\frac{\left[N_2(X,v=0) \right] \times Q_{rot}^{N_2(X,v=0)}(T_r)}{\left[N_2(X,v) \right] \times Q_{rot}^{N_2(X,v)}(T_r)} \right) \quad (30)$$

The normalized vibrational temperature η_v is defined in such a way that it is equal to 0 when $T_v(v) = T_g$ and to 1 when $T_v(v) = T_e$.

The results plotted in Figure 44 confirm the foregoing analysis. Before the jump (T_e = 5000 K), T_v is practically equal to T_g. During the jump (T_e = 9800 K), T_v takes values

between T_g and T_e. After the jump (T_e = 12,000 K), T_v is very close to T_e, except for high-lying vibrational levels.

4.7. Conclusion

A new kinetic model and an improved collisional-radiative (CR) model were presented for nonequilibrium nitrogen plasmas in which electrons and heavy-species have Maxwellian velocity distribution functions at different temperatures. In both models, the dependence of rate coefficients on the different kinetic (T_e, T_g) and population (T_{el}, T_v, T_r) temperatures is rigorously accounted for. The kinetic model is based on the assumption that internal energy levels of atoms and molecules are populated according to Boltzmann distributions at temperatures T_{el}, T_v, and T_r, and can only be used to predict total concentrations of chemical species. The CR model assumes only that the rotational levels follow a Boltzmann distribution at temperature T_r, and allows for the calculation of vibronic level populations.

Predictions of the CR model under conditions of chemical nonequilibrium were compared with the N_2 B state vibrational level population measurements reported by Gessman *et al.* [2, 94]. Good agreement was found after small adjustments of a few controlling rates that remained within experimental uncertainties on corresponding cross-sections.

The CR and the kinetic models were both employed to study nitrogen plasmas in thermal nonequilibrium. It was found that, depending on the electron temperature T_e, a transition takes place between a regime in which vibrational molecular levels are equilibrated by collisions with heavy species and a regime where they are equilibrated by collisions with electrons. It follows that kinetic models can be used to accurately predict the chemical composition of nonthermal plasmas, at least under steady-state conditions, provided that the vibrational regime is known *a priori*.

5. Publications

Packan, D.M., Gessman, R.J., Pierrot, L., Laux, C.O., and Kruger, C.H., "Measurement and Modeling of OH, NO, and CO2 Infrared Radiation in a Low Temperature Air Plasma," Journal of Thermophysics and Heat Transfer, to be submitted, 2001.

Yu, L, Pierrot, L., Laux, C.O., and Kruger, C.H., "Effects of Vibrational Nonequilibrium on the Chemistry of Two-Temperature Nitrogen Plasmas," Plasma Chemistry and Plasma Processing, in press, 2001.

Jenniskens, P., Wilson, M.A., Packan, D., Laux, C.O., Kruger, C.H., Boyd, I.D., Popova, O.P., and Fonda, M., "Meteors: A Delivery Mechanism of Organic Matter to the Early Earth," Earth, Moon and Planets, Vol. 82-83, p. 57-70, 2000

Laux, C.O., Gessman, R.J., Kruger, C.H., Roux, F., Michaud, F., and Davis, S.P., "Rotational Temperature Measurements in Air and Nitrogen Plasmas Using the First Negative System of

Laux, C.O., Gessman, R.J., Kruger, C.H., Roux, F., Michaud, F., and Davis, S.P., "Rotational Temperature Measurements in Air and Nitrogen Plasmas Using the First Negative System of N2+," Journal of Quantitative Spectroscopy and Radiative Transfer, Vol. 68, No. 4, pp. 473-482, 2001.

Michaud, F., Roux, F., Davis, S.P., Nguyen, A.-D., and Laux, C.O., "High-Resolution Fourier Spectrometry of the N2+ ion," Journal of Molecular Spectroscopy, Vol. 203, pp. 1-8, Sept. 2000.

Levin, D.A., Laux, C.O, and Kruger, C.H., "A General Model for the Spectral Calculation of OH Radiation in the Ultraviolet," Journal of Quantitative Spectroscopy and Radiative Transfer, Vol. 61 (3), pp. 377-392, 1999.

Jenniskens, P, de Lignie, M., Betlem, H., Borovicka, J., Laux, C.O., Packan, D., and Kruger, C.H., "Preparing for the 1998/1999 Leonid Storms," contributed Chapter in Laboratory Astrophysics and Space Research, pp. 425-455, P. Ehrenfreund, H. Kochan (eds.), Kluwer Academic Publishers, 1999.

Jenniskens, P, de Lignie, M., Betlem, H., Borovicka, J., Laux, C.O., Packan, D., and Kruger, C.H., "Preparing for the 1998/1999 Leonid Storms," Earth, Moon and Planets Vol. 80, pp. 311-341, 1998.

Pierrot, L., Laux, C.O., and Kruger, C.H., "Consistent Calculation of Electron-Impact Electronic and Vibronic Rate Coefficients in Nitrogen Plasmas," Progress in Plasma Processing of Materials, pp. 153-159, Begell House, Inc., NY, 1999.

Kruger, C.H., Owano, T.G., Laux, C.O., and Zare, R.N., "Nonequilibrium in Thermal Plasmas," Journal de Physique IV, Vol. 7, pp. C4-77–C4-92, 1997.

Kruger, C.H., Owano, T.G., and Laux, C.O., "Experimental Investigations of Atmospheric Pressure Nonequilibrium Plasma Chemistry," Invited submission to the special issue "High Pressure Arcs and High Frequency Thermal Plasmas," IEEE Transactions on Plasma Science, Vol. 25, No. 5, pp. 1042-1051, 1997.

Laux, C.O., "Glow Discharges in Atmospheric Pressure Air," Gordon Research Conference on Plasma Processing Science, Tilton, NH, August 13-18, 2000 (invited).

Nagulapally, M, Candler, G.V., Laux, C.O., Yu, L., Packan, D., Kruger, C.H., Stark, R., Schoenbach, K.H., "Experiments and Simulations of DC and Pulsed Discharges in Air Plasmas," *AIAA 2000*-2417, 31st AIAA Plasmadynamics and Lasers Conference, Denver, CO, June 19-22, 2000.

Laux, C.O., Yu, L., Packan, D.M., Pierrot, L., Kruger, C.H., and Zare, R.N., "Experimental and theoretical investigations of ionization mechanisms in air plasma discharges at atmospheric pressure," Gaseous Electronics Conference, Norfolk, VA, October 5-8, 1999.

Candler, G.V., Nagulapally, M., Laux, C.O., and Kruger, C.H., "Numerical Simulation of a Constant Current Density Discharge in a Flowing Plasma," Gaseous Electronics Conference, Norfolk, VA, October 5-8, 1999.

Yu, L, Pierrot, L., Laux, C.O., and Kruger, C.H., "Effects of Vibrational Nonequilibrium on the Chemistry of Two-Temperature Nitrogen Plasmas," Proceedings of the 14th International Symposium on Plasma Chemistry, pp. 1079-1085, Prague, Czech Republic, August 2-6, 1999.